

Spacetime Spins: Statistical mechanics for error correction with stabilizer circuits

Cory T. Aitchison¹ and Benjamin Béri^{1,2}

¹DAMTP, University of Cambridge, Wilberforce Road, Cambridge, CB3 0WA, UK

²T.C.M. Group, Cavendish Laboratory, University of Cambridge, J.J. Thomson Avenue, Cambridge, CB3 0HE, UK

A powerful method for analyzing quantum error-correcting codes is to map them onto classical statistical mechanics models. Such mappings have thus far mostly focused on static codes, possibly subject to repeated syndrome measurements. Recent progress in quantum error correction, however, has prompted new paradigms where codes emerge from stabilizer circuits in spacetime—a unifying perspective encompassing syndrome extraction circuits of static codes, dynamically generated codes, and logical operations. We show how to construct statistical mechanical models for stabilizer circuits subject to independent Pauli errors, by mapping logical equivalence class probabilities of errors to partition functions using the spacetime subsystem code formalism. We also introduce a modular language of spin diagrams for constructing the spin Hamiltonians, which we describe in detail focusing on independent circuit-level X - Z error channels. With the repetition and toric codes as examples, we use our approach to analytically rank logical error rates and thresholds between code implementations with standard and dynamic syndrome extraction circuits, describe the effect of transversal logical Clifford gates on logical error rates, and perform Monte Carlo simulations to estimate maximum likelihood thresholds. Our framework offers a universal prescription to analyze, simulate, and compare the decoding properties of any stabilizer circuit, while revealing the innate connections between dynamical quantum systems and noise-resilient phases of matter.

I. INTRODUCTION

Quantum error-correction (QEC) enables quantum computers to operate reliably despite the presence of noise [1–11]. The simplest QEC setting is that of a quantum memory, robustly storing logical information via repeated rounds of syndrome extraction. Quantum computation then evolves this with fault-tolerant logical operations that limit the accumulation of errors.

Quantum memories exemplify noise-resilient phases of matter [5, 12–38]: The probability of logical errors, given a code and noise model, can be directly expressed through partition functions of statistical mechanical (SM) Ising models [5]. The error threshold—a critical physical error rate, below which increasing the number of physical qubits leads to a lower logical error rate [1–7]—then emerges as a phase transition between ordered (error correcting) and disordered (non-correcting) phases. Identifying these phase boundaries allows one to assess the theoretical, decoder-agnostic, memory limits.

An important emerging frontier concerns how concepts of phases of matter can capture inherently dynamical aspects of fault tolerance, e.g., syndrome-extraction circuits, logical operations for quantum computations, or indeed intrinsically dynamic codes [39–71]. In this paper, we address this question by showing how to construct SM models for stabilizer circuits—with elementary Clifford gates, resets, and measurements, furnishing the most general fabric behind fault-tolerant constructions.

Leveraging stabilizer dynamics is of increasing focus in practical QEC [62–65, 72–85]; examples include designing circuits to overcome hardware limitations [74, 75], avoid qubit or coupler dropouts [76–79], reduce overheads [80], or turn a static threshold-less code into a dynamical code with thresholds [81]. Despite these advancements, except for approaches specific to certain

codes or circuits [41, 48, 49, 51], or cases where time describes repeated syndrome measurement in phenomenological models [5, 15], SM mappings have largely focused on static codes. Our SM models for stabilizer circuits fill this important gap.

In the dynamic setting, QEC and quantum computations correspond to $(d+1)$ -dimensional $[(d+1)D]$ circuits. Our SM models first represent these as related stabilizer subsystem codes in $(d+1)$ -spatial dimensions, known as spacetime codes [61, 65, 85–88]. Considering generic uncorrelated Pauli noise channels, we then construct a classical Hamiltonian whose partition function—by summing over related error configurations—accounts for fundamental error thresholds and the lowest achievable logical error rates; our SM models are thus of the same status for the dynamical settings as traditional SM models have been for quantum memories.

Mapping stabilizer circuits onto SM models opens up new avenues for analysis beyond those seen in the static case. This framework allows us to compare different compilations of the syndrome-measurement circuits of a QEC code, for example. It also enables statistical mechanical analysis of the logical circuits, such as through transversal gates, lattice surgery, or code switching. A circuit-based analysis of decodability introduces spatially-correlated noise processes—such as “hook errors” from CNOTs between ancilla and data qubits [82, 84]—absent from abstracted phenomenological representations of QEC syndrome measurements. These processes are naturally captured by our SM models. Moving SM mappings beyond static codes thus provides useful practical features, beyond its key role in a holistic understanding of fault tolerance and how this defines noise-resilient dynamic phases of matter.

A central technical ingredient in our approach is the introduction of modular spin diagrams, a graphical lan-

guage of elementary building blocks for constructing SM models for stabilizer circuits. While usable with general noise models, this approach is particularly simple for independent circuit-level X - Z noise (where independent X and Z errors can occur before or after any stabilizer operation in the circuit), for which the SM Hamiltonians can be systematically simplified by integrating out certain spins. The spin diagrams we introduce have similarities with those used in ZX-calculus [89, 90] with Pauli flows [67, 72]; a core difference is that our spin diagrams encode the noise channel, ensuring that simplifying the diagrams preserves the SM partition functions. (See also Ref. [91] for a related construction that uses ZX-diagrams to manipulate circuits while preserving the effects of faults, and Ref. [87] for an approach with similar simplification processes but in the context of chain complexes.)

The rest of the paper is structured as follows: Section II presents a brief background on QEC and spacetime codes. Section III outlines the spin models and diagrams for stabilizer circuits. We then apply this to several demonstrative examples. First, in Sec. IV, we study the 1D repetition code, including different syndrome extraction circuits and logical CNOT operations. These examples will help convey the workings of our approach in the simplistic settings of 2D random bond Ising models. In Sec. V we then study the toric code and show how our approach can describe and make qualitative predictions about the performance of recently introduced dynamic syndrome extraction schemes [42, 66, 74, 75] compared with standard syndrome extraction circuits. We conclude and provide future directions in Sec. VI. The appendices contain derivations and details of the numerical methods.

II. PRELIMINARIES

In this section, we present a brief introduction to the theory of quantum error-correcting codes, and how decoding of circuits can be mapped onto spacetime codes.

A. Error-correcting codes

Error-correcting codes are designed to protect encoded logical quantum information. In this paper we use subsystem codes [12], which are generalizations of stabilizer codes [1–3, 6, 8–11] and arise naturally in the spacetime code formalism [61, 65, 85–88]. Information is encoded in a codespace \mathfrak{C} : the simultaneous $+1$ -eigenspace of a group \mathcal{S} of commuting Pauli operators, “stabilizers”,

$$\mathcal{S} = \langle S_1, S_2, \dots, S_k, \dots, S_\kappa \rangle, \quad -I \notin \mathcal{S}. \quad (1)$$

\mathcal{S} is the center of a larger gauge group, \mathcal{G} , which may contain non-commuting elements. The members of \mathcal{G} are called gauge operators. Logical operators commute with all stabilizers, but are not themselves in \mathcal{G} . For Pauli operators A, B , define the scalar commutator $\llbracket A, B \rrbracket \in$

$\{-1, 1\}$ by the relation

$$AB = \llbracket A, B \rrbracket BA. \quad (2)$$

If \mathfrak{C} is 2^l -dimensional, then there exist l pairs of logical \bar{X}_i, \bar{Z}_i operators that act as Pauli X and Z on \mathfrak{C} , with anticommutation relation

$$\llbracket \bar{X}_i, \bar{Z}_j \rrbracket = (-1)^{\delta_{ij}}. \quad (3)$$

Each \bar{X}_i, \bar{Z}_i pair defines a logical qubit that encodes logical information. If a logical operator commutes with all the gauge operators, it is known as a bare logical operator; otherwise, it is a dressed logical operator. The anticommutation relation, Eq. (3), must hold for bare logicals, but may not hold for dressed logicals.

These codes protect the logical state by signalling when (and information on where) an error occurs. Specifically, for N -qubit density matrix ρ , we consider single-qubit Pauli error channels,

$$\mathcal{E} = \bigotimes_{i=1}^N \mathcal{E}_i, \quad \mathcal{E}_i[\rho] = \sum_{\alpha \in \mathcal{P}_i} \mathbb{P}(\alpha) \alpha \rho \alpha^\dagger, \quad (4)$$

where $\mathcal{P}_i = \{I, X, Y, Z\}$ are the single-qubit Pauli operators (modulo phase) for qubit i . $\mathbb{P}(\alpha)$ is the probability of an α -error on a qubit. We shall use the same error channel during each timestep of a circuit, for simplicity.¹ In the absence of errors, a stabilizer measurement returns $+1$. Errors anticommute with some S_k , and thus produce a syndrome, $\mathbf{s} \in \{-1, 1\}^N$ for the stabilizer measurement outcomes. Given a syndrome, a decoder is an algorithm that outputs a correction Pauli operator $C_{\mathbf{s}}$. An error E with syndrome \mathbf{s} is successfully corrected if $EC_{\mathbf{s}} \in \mathcal{G}$, i.e., $E \in C_{\mathbf{s}}\mathcal{G}$; otherwise, $EC_{\mathbf{s}} \in L\mathcal{G}$ (i.e., $E \in C_{\mathbf{s}}L\mathcal{G}$) where $L \in \{\bar{X}, \bar{Z}, \dots\}$ is a nontrivial logical operator, and a logical error occurs. These $L\mathcal{G}$ are logical equivalence classes or error cosets.

The optimal decoder—known as the maximum-likelihood (ML) decoder—outputs the $C_{\mathbf{s}}$ whose error coset has the highest probability. The success probability of a decoder is

$$\mathbb{P}(\text{success}) = \sum_{\mathbf{s}} \mathbb{P}(\mathbf{s}) \mathbb{P}(\text{success}|\mathbf{s}), \quad (5)$$

where $\mathbb{P}(\mathbf{s})$ is the probability of observing a syndrome \mathbf{s} . The conditional probability of success is

$$\mathbb{P}(\text{success}|\mathbf{s}) = \frac{\mathbb{P}(\overline{C_{\mathbf{s}}})}{\sum_{L \in \{I, \bar{X}, \bar{Z}, \dots\}} \mathbb{P}(\overline{C_{\mathbf{s}}L})}, \quad (6)$$

where the probability of an error coset $\overline{E} = E\mathcal{G}$ is

$$\mathbb{P}(\overline{E}) = \sum_{\epsilon \in E\mathcal{G}} \mathbb{P}(\epsilon), \quad (7)$$

¹ Our results are readily generalizable to location or time-dependent error models, but for notational simplicity we restrict attention to translation-invariant channels in this work.

and L are representative logical errors. The ML decoder chooses a C_s such that its coset probability is greater than all other cosets with the same syndrome,

$$\mathbb{P}(\overline{C_s}) > \max \left\{ \mathbb{P}(\overline{C_s \bar{X}}), \mathbb{P}(\overline{C_s \bar{Z}}), \dots \right\}. \quad (8)$$

This maximizes $\mathbb{P}(\text{success}|\mathbf{s})$. Below the error threshold, the success probability of an ML decoder approaches 1 as the code size (i.e., the code distance) increases.

B. Spacetime codes

The codes described above protect information in a static quantum memory. Quantum computation, however, requires a quantum state to evolve via the unitaries and measurements of a quantum circuit. The spacetime code formalism allows us to interpret this dynamical state as a static subsystem code—the spacetime code—in one higher spatial dimension [61, 65, 85–88].² A decoder of the spacetime code can be used to construct an equivalently-performing decoder for the corresponding circuit. We present here a brief overview of spacetime codes; for more detail we refer the reader to Delfosse and Paetznick [85].

We assume a Clifford circuit of N physical qubits: at every timestep $t = 0, 1, \dots, T$ each qubit is either measured with a Pauli operator or is acted on by a Clifford unitary (which may be the identity). This enforces that all measurements and unitaries at the same timestep have disjoint support and thus commute with each other. In-between each timestep, an error channel, cf. Eq. (4), acts on the physical qubits; we say that errors occur at half-integer times $\tau = 0.5, 1.5, \dots, T - 0.5$. Although this error model does not explicitly include measurement errors, they occur implicitly whenever an error at time τ anticommutes with a measurement at $\tau + 0.5$; this captures the essential features of circuit-level noise without a separate measurement noise parameter. Independent measurement errors may be incorporated by having an additional spacetime qubit attached to each measurement and subjected to bit-flip errors with probability p_{meas} .³

To construct the spacetime code, we model a Hilbert space of NT so-called spacetime qubits, each labeled by a coordinate (i, τ) where $i = 1, \dots, N$ corresponds to the location of physical qubit and τ is the half-integer time. If an error in the circuit occurs on qubit $i = 3$ between times $t = 2$ and $t = 3$, for example, it occurs on the spacetime qubit at $(i, \tau) = (3, 2.5)$.

Let \mathcal{P}_{ph} and \mathcal{C}_{ph} be the group of Pauli and Clifford operators acting on the N physical qubits of the circuit, and \mathcal{P}_{st} and \mathcal{C}_{st} those acting on the NT spacetime qubits. For

$U \in \mathcal{C}_{\text{ph}}$, the notation $[U]_{\mathcal{I}, \tau} \in \mathcal{C}_{\text{st}}$ denotes the spacetime operator that acts on qubits $i \in \mathcal{I}$ at half-integer time τ , and the identity elsewhere. For example, $[XZ]_{\{i, j\}, \tau}$ is a Pauli X on qubit i and a Z on qubit j at half-integer time τ . When the support is clear from the operator itself, we write simply $[U]_{\tau}$.

The spacetime code is a subsystem code; the gauge group defines equivalences between errors in spacetime that have the same effects on the circuit (syndromes and logical operator outcomes). The gauge group is typically generated by two types of spacetime operators [85]:

1. $[M_i]_{t_i-0.5}$ and $[M_i]_{t_i+0.5}$, for each measurement $M_i \in \mathcal{P}_{\text{ph}}$ at integer time t_i . These encode that the qubits will be in an eigenstate of M_i at time t_i .
2. $[Q]_{t_i-0.5} [\mathcal{U}_{t_i} Q \mathcal{U}_{t_i}^\dagger]_{t_i+0.5}$, for each operator $Q \in \mathcal{P}_{\text{ph}}$ that commutes with all M_i at integer time t_i . Here, $\mathcal{U}_{t_i} \in \mathcal{C}_{\text{ph}}$ is the product of all unitaries that act at time t_i . These generators encode how errors propagate through the circuit.

If qubit i is not measured at time t , any single-qubit Pauli on qubit i commutes with the measurements at t . The second type of generator is then just

$$[X]_{i, t-0.5} [\mathcal{U}_t X \mathcal{U}_t^\dagger]_{i, t+0.5}, \quad [Z]_{i, t-0.5} [\mathcal{U}_t Z \mathcal{U}_t^\dagger]_{i, t+0.5}. \quad (9)$$

We explain in more details the spacetime stabilizers and logical operators in Appendix A 1; their precise form is not needed for the construction of the spin models. In brief, the stabilizers correspond to detector cells: products of measurement outcomes that are deterministic in the absence of errors, and thus reveal where errors occur. The bare logical operators are concatenations of an initial logical operator's images under the circuit at each timestep; for a 1D string logical operator on a topological code, for example, a fault-tolerant Clifford circuit extends these to 2D membranes in spacetime. These bare logical operators obey the anticommutation relation, Eq. (3), whereas dressed logicals (such as the image of a code's \bar{X} at a particular timestep) may not. (Operators at different timesteps, for example, always commute).

III. SPACETIME SPIN MODELS

A powerful property of quantum codes is that the probabilities of error cosets can be related to statistical mechanics; models that delineate the limits up to which QEC can work and encapsulate fundamental notions of noise-resilient phases of matter. Initially introduced by Dennis *et al.* [5] for uncorrelated Pauli errors in the toric code, such SM mappings have since encompassed, for example, more stabilizer codes [13–15], subsystem codes [12], coherent errors [18, 20–23], and post-selection [26, 93]. We now describe this mapping for general Clifford circuits—extending beyond static codes—subject to noise channels of the form in Eq. (4). In

² Although the main results of Delfosse and Paetznick [85] are for spacetime stabilizer codes, their construction also applies to spacetime subsystem codes, as we shall use here.

³ This approach was used in Gidney *et al.* [92], for example.

Sec. III C, we show how to represent these SM models as spin diagrams that can be constructed modularly for each circuit element. These diagrams are particularly simple when restricted to independent X - Z noise channels. Section III D formalizes the process of simplifying diagrams by removing low-connectivity spins. For a more detailed derivation of this formulation, see Appendix A 2.

We wish to express the probability of an error coset, $\mathbb{P}(\overline{E})$, as a partition function, \mathcal{Z}_E . To enumerate all errors in the coset $E\mathcal{G}$, we multiply the representative error E by all possible gauge group elements $g \in \mathcal{G}$. We relate this to the SM model by assigning an Ising spin $\sigma_k \in \{-1, 1\}$ to each gauge generator g_k ; we include g_k in g if $\sigma_k = -1$. The spin configuration $\sigma = [\sigma_1, \sigma_2, \dots, \sigma_m]$ thus specifies a group element

$$g(\sigma) = \prod_{k=1}^m g_k^{(1-\sigma_k)/2} \in \mathcal{G}. \quad (10)$$

Interaction signs

$$\eta_{i,\tau}(\alpha) \equiv \llbracket [\alpha]_{i,\tau}, E \rrbracket \quad (11)$$

encode the reference string E and will create quenched disorder. An important property is that for any error $\epsilon = Eg(\sigma)$ in the coset, the product $\eta_{i,\tau}(\alpha) \prod_k \sigma_k$, over all k where $\llbracket [\alpha]_{i,\tau}, g_k \rrbracket = -1$, equals +1 if ϵ commutes with $[\alpha]_{i,\tau}$, and -1 if it anticommutes. We use this product to assign ϵ the correct probability via dimensionless interaction strengths $K_{i,\tau}(\alpha)$ that weight each product such that e^{-H_E} equals $\mathbb{P}(\epsilon)$ (with H_E a dimensionless Hamiltonian).⁴ Their value is specified by the noise channel, cf. Eq. (4), via a Nishimori condition (see Appendix A 2),

$$K_{i,\tau}(\alpha) = \frac{1}{4} \sum_{Q \in \mathcal{P}} \ln[\mathbb{P}(Q)] \llbracket [\alpha]_{i,\tau}, [Q]_{i,\tau} \rrbracket, \quad (12)$$

where $\mathcal{P} = \{I, X, Y, Z\}$.⁵ Combining these components together, we have

$$\mathbb{P}(\overline{E}) = \sum_{\sigma} \mathbb{P}[Eg(\sigma)] \equiv \sum_{\sigma} e^{-H_E} = \mathcal{Z}_E \quad (13)$$

with Hamiltonian

$$H_E = - \sum_{i=1}^N \sum_{\tau=0.5}^{T-0.5} \sum_{\alpha \in \mathcal{P}} K_{i,\tau}(\alpha) \eta_{i,\tau}(\alpha) \prod_{k: \llbracket [\alpha]_{i,\tau}, g_k \rrbracket = -1} \sigma_k. \quad (14)$$

To illustrate the interactions in H_E , consider two examples: **Idling:** If qubit i idles at time t , then by

Eq. (9) there are two relevant gauge generators $g_1 = [X]_{i,t-0.5}[X]_{i,t+0.5}$ and $g_2 = [Z]_{i,t-0.5}[Z]_{i,t+0.5}$. The spin σ_1 associated with g_1 interacts via $K_{i,t\pm 0.5}(\alpha) \eta_{i,t\pm 0.5}(\alpha)$ for $\alpha = Y, Z$, and similarly for σ_2 for $\alpha = X, Y$. **Measurements:** If qubit i is instead measured in the Z basis at time t , then we have gauge generators $g_3 = [Z]_{i,t-0.5}$ and $g_4 = [Z]_{i,t+0.5}$. It is possible to construct a basis such that these are the only two Z -flavored generators acting on qubits $(i, t \pm 0.5)$ and the interactions via $K_{i,t\pm 0.5}(X) \eta_{i,t\pm 0.5}(X)$ are field terms.

A. Decoding

Since $\mathcal{Z}_E = \mathbb{P}(\overline{E})$ for each logical equivalence class, maximum-likelihood decoding, Eq. (8), reduces to finding the coset with maximum partition function—equivalently, minimum free energy $F_E = -\ln \mathcal{Z}_E$ —consistent with the syndrome [94]. The success probability of a decoder, Eq. (6), can be expressed as a (softmax) function of these free energies,⁶

$$\mathbb{P}(\text{success}|\mathbf{s}) = \frac{e^{-F_{C_s}}}{\sum_L e^{-F_{C_s L}}}. \quad (15)$$

Below threshold, the free-energy diverges in the thermodynamic limit for all $C_s L$ ($L \neq I$, and C_s the ML Pauli correction) as the ML success probability goes to 1 [15]. Ordered phases of matter are typically characterized by long-range correlations and extensive free-energy costs associated with introducing macroscopic domain walls; the error threshold generally coincides with ordered-disordered phase transitions in the SM model [5, 15].

The logical classes that are summed over in Eq. (15) depend on the spacetime code and its underlying circuit. A static code that supports l logical qubits has 2^{2l} logical equivalence classes for each syndrome ($C_s \mathcal{G}, \bar{X}_1 C_s \mathcal{G}, \bar{Z}_1 C_s \mathcal{G}, \dots$) with coset representatives given by combinations of the logical operators of the code. When a code is compiled into a syndrome-extraction circuit and mapped onto a spacetime code, additional logical equivalence classes may arise.

For example, in a stability experiment [95], one constructs a syndrome-extraction circuit and tests the ability for a decoder to predict the parity of a product of stabilizers after being subjected to errors. A decoder will certainly fail if an error occurs that flips this parity but does not alter the syndrome; one such error is a timelike string of errors that extends across the whole duration of the experiment (cf. Fig. 4b). These undetected timelike errors are coset representatives of some of the spacetime code's logical equivalence classes. In stability

⁴ For simplicity, we work with dimensionless quantities. One can equivalently define $J_{i,\tau}(\alpha) = K_{i,\tau}(\alpha)/k_B T$, where T is a temperature to instead use a Hamiltonian in units of energy.

⁵ When some $\mathbb{P}(\epsilon) = 0$, this equation is not defined; however, by by taking appropriate limits and using the convention $\exp(\ln 0) = 0$, the formalism remains well-defined [15].

⁶ There is not a unique basis for \mathcal{G} and so the Hamiltonian is basis-dependent; the free energy and probability ratios, however, are independent of the basis.

experiments, one typically uses spatial boundary conditions such that no logical qubit is encoded: the code's \bar{X} and \bar{Z} anticommute with stabilizers on the boundary and do not form logical equivalence classes. The decoder now chooses between only the trivial logical equivalence class \mathcal{G} and those with undetected timelike errors. In contrast, in a memory experiment, one tests the ability for a decoder to preserve the state of an encoded logical qubit by asking it to predict the final eigenvalue of a logical operator after the circuit and comparing it with the true value. Undetected timelike errors add logical equivalence classes and increase the complexity of decoding; one therefore typically uses temporal boundary conditions with spacetime stabilizers that anticommute with these spanning timelike errors to focus on the effect of the static code's logical equivalence classes. Memory and stability experiments are discussed further in Sec. IV A, using the repetition code as a guiding example.

B. Independent X-Z noise

The above prescription holds for any noise channel. Under an independent X - Z noise channel,

$$\begin{aligned} \mathbb{P}(I) &= (1 - p_X)(1 - p_Z), \quad \mathbb{P}(X) = p_X(1 - p_Z), \\ \mathbb{P}(Y) &= p_X p_Z, \quad \mathbb{P}(Z) = (1 - p_X)p_Z \end{aligned} \quad (16)$$

with $p_X, p_Z \in [0, 1]$,⁷ the Nishimori conditions become

$$K(I) = \frac{1}{2} \ln(p_X p_Z (1 - p_X)(1 - p_Z)), \quad (17)$$

$$K(X) = \frac{1}{2} \ln\left(\frac{1 - p_Z}{p_Z}\right) \equiv K_Z, \quad (18)$$

$$K(Y) = 0, \quad (19)$$

$$K(Z) = \frac{1}{2} \ln\left(\frac{1 - p_X}{p_X}\right) \equiv K_X. \quad (20)$$

We use the swapped subscripts on K_X and K_Z to increase interpretability: K_α interaction strengths account for the probability of α -errors. Hamiltonian to separate into X and Z contributions. The Hamiltonian's interaction signs are sampled from independent Bernoulli distributions, where

$$\eta_{\alpha,(\iota,\tau)} \sim 1 - 2\text{Bernoulli}(p_\alpha) \equiv \begin{cases} \mathbb{P}(\eta = 1) = p_\alpha \\ \mathbb{P}(\eta = -1) = 1 - p_\alpha \end{cases} \quad (21)$$

for every qubit i and $\alpha = X, Z$. Ignoring the constant contribution to the Hamiltonian from the $\alpha = I$ terms,

Eq. (14) is then written as

$$\begin{aligned} H_E &= H_{X,E} + H_{Z,E}, \\ H_{\alpha,E} &= -K_\alpha \sum_{i=1}^N \sum_{\tau=0.5}^{T-0.5} \eta_{\alpha,(\iota,\tau)} \prod_{k: [[\tilde{\alpha}]_{i,\tau}, g_k] = -1} \sigma_k, \end{aligned} \quad (22)$$

where $\tilde{\alpha}$ denotes the opposite Pauli: $\tilde{X} = Z$ and $\tilde{Z} = X$; recall $K(X) \equiv K_Z$ and $K(Z) \equiv K_X$. For CSS spacetime codes—where every gauge generator has pure X or pure Z support—each spin appears in only one of H_X or H_Z . The partition function, Eq. (13), then factors into $\mathcal{Z}_E = \mathcal{Z}_{X,E} \mathcal{Z}_{Z,E}$ where

$$\mathcal{Z}_{\alpha,E} = \sum_{\sigma} e^{-H_{\alpha,E}}. \quad (23)$$

C. Spin diagrams

One of our central results is to provide a framework to systematically construct these Hamiltonians using spin diagrams: a graphical language where each circuit element—idle wires, CNOTs, measurements, etc.—contributes standard “building blocks” of spins and interactions. These diagrams both enable constructing models for arbitrary Clifford circuits, and reveal connections to established lattice models. Spin diagrams work for general noise channels; here we demonstrate them for independent circuit-level X - Z noise, where they are particularly transparent. For general noise channels, each spin has more interactions, which are harder to visualize.

We construct each diagram by drawing a square for each spin σ_k , and connect red (blue) lines for each field term, bond, or many-body interaction in $H_{X,E}$ ($H_{Z,E}$). The number of lines attached to a spin are the number of interactions it participates in through the Hamiltonian—we refer to this as the degree of the spin. Figure 1 illustrates some of these building blocks. An idling qubit, for example, contributes two generators and therefore two spins, one for H_X (red) and one for H_Z (blue). A CNOT gate couples together spins on adjacent qubits. Composing these building blocks together, we can represent a circuit as a spin diagram, such as in Fig. 2.

Many of these spins can be eliminated, producing a simpler—but equivalent—Hamiltonian: Spins with a single interaction, arising around single-qubit resets and measurements, correspond to gauge operators that identify single-qubit errors with no effect on the syndrome or logical operators. Spins with exactly two interactions, such as those found on idling qubits, encode gauge-equivalent pairs of single-qubit errors at different spacetime locations that can be grouped together. Both cases can be integrated out, simplifying the model while preserving the partition function up to an E -independent multiplicative factor; relevant physical quantities like probability ratios $\mathbb{P}(\bar{E})/\mathbb{P}(\bar{E}')$, free-energy differences

⁷ If a $p_\alpha = 0$, care needs to be taken to ensure interactions involving $K_\alpha \rightarrow \infty$ are satisfied. In CSS codes, this usually involves removing all α -flavored generators, and ignoring $H_{\alpha,E}$.

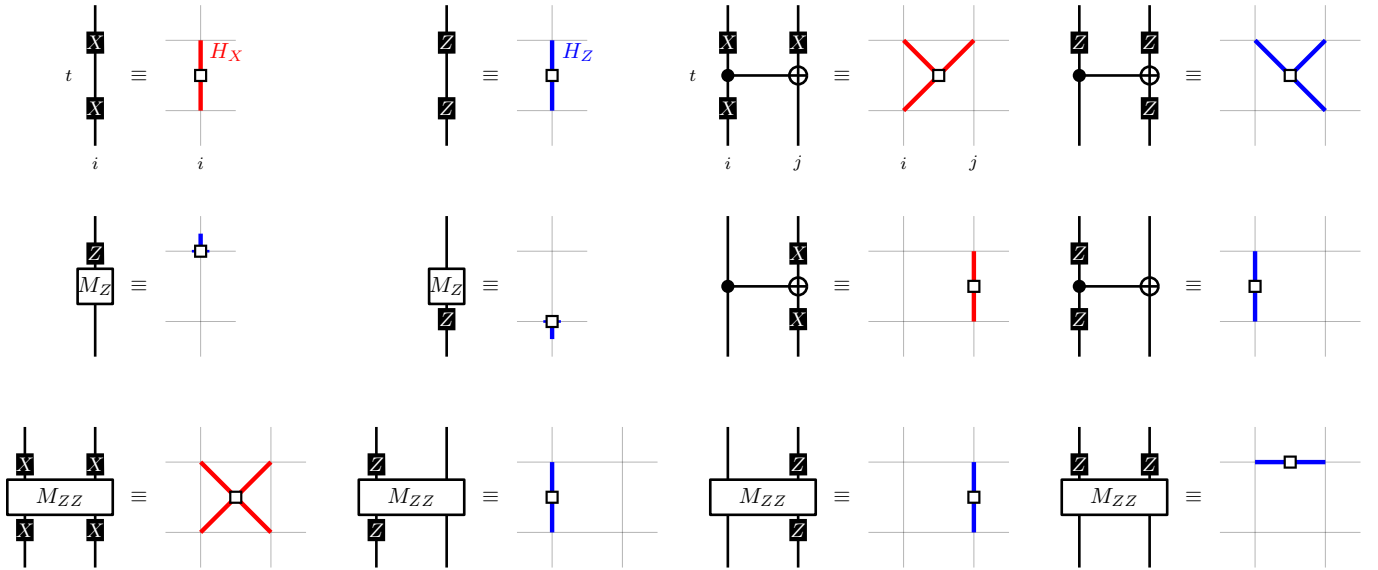


Figure 1. The gauge generators (black labels) introduced by various Clifford gates and corresponding spin model ingredients. Each generator is associated with a spin (white square); interactions (colored lines) connect spins according to Eq. (22). Red and blue lines are interactions on H_X and H_Z respectively. Gridlines show the spacetime locations (i, τ) , with time going up the page. A qubit i idling at integer time t , introduces two gauge generators: $[X]_{i,t-0.5}[X]_{i,t+0.5}$ and $[Z]_{i,t-0.5}[Z]_{i,t+0.5}$. A CNOT has four gauge generators; $g_1 = [X]_{i,t-0.5}[XX]_{\{i,j\},t+0.5}$ acts on three spacetime qubits and hence its spin has three legs (interactions). A single-qubit measurement M_Z (a single-qubit reset, R_Z , produces the same spins and interactions) has gauge generators with only one interaction in H_Z so we draw its spins atop the corresponding spacetime qubit. M_Z introduces no spins to H_X (and similarly for M_X and H_Z). Two-qubit measurements M_{ZZ} introduce a spin with four interactions and three spins with two-interactions. Shown here is one basis choice; $[ZZ]_{\{i,j\},t-0.5}$ could also have been used instead of $[ZZ]_{\{i,j\},t+0.5}$.

$\Delta F = -\ln \mathcal{Z}_E + \ln \mathcal{Z}_{E'}$, and thus ML decoding decisions remain unchanged. To preserve the partition function, each interaction must now be assigned a weight equal to the number of single-qubit errors grouped together as gauge-equivalent. This weight determines the interaction's effective coupling strength K and the probability distribution of its sign η , see Eqs. (25) and (26) in Sec. III D, with additional details in Appendix A 2 a. We illustrate this simplification on a spin diagram corresponding to the ZZ measurement circuit in Fig. 2.

Using this prescription, we can identify common circuits elements with their spin diagrams, as in Fig. 3. Each diagram can be composed with others to form a full circuit spin diagram and thus the Hamiltonian, bypassing the computation of gauge generators and anticommutations. When composing circuit elements, interactions of weight w_1 and w_2 that merge form a new interaction of weight $w_1 + w_2 - 1$ (since one spacetime location is shared). In Sections IV and V, we use these building blocks to construct SM models for a variety of examples.

D. Gauge-equivalent components

Having illustrated spin integration graphically, we now describe the precise form of the simplified Hamiltonian. Appendix A 2 a formalizes the mathematical process be-

hind integrating and re-weighting interactions, which is applicable to generic noise channels (Hamiltonians of the form in Eq. (14)). However, under independent X - Z noise the integration process allows the Hamiltonian to take on a particularly simple and interpretable form.

To write down the Hamiltonian, we first identify grouped interactions terms in the integrated Hamiltonian with connected components in a related vertex-labeled graph. Specifically, we construct the graph $\Gamma = (V, E, L)$ where $V = \{1, 2, \dots, 2NT\}$ are vertices (representing interactions in the unintegrated Hamiltonian), E are edges (defined below), and $L : V \xrightarrow{\text{bijective}} \{X, Z\} \times \{1, 2, \dots, N\} \times \{0.5, \dots, T-0.5\}$ labels each vertex by a unique Pauli flavor and spacetime qubit. Then:

1. For every single-qubit generator $g_k = [\alpha]_{i,\tau}$, remove from Γ the vertex v with $L(v) = (\alpha, i, \tau)$.
2. For every generator $g_k = [\alpha]_{i,\tau}[\alpha']_{i',\tau'}$, where $\alpha, \alpha' = X$ or Z , add an edge (v, v') to E that joins vertices $v = L^{-1}(\alpha, i, \tau)$ and $v' = L^{-1}(\alpha', i', \tau')$.
3. Form connected components $c \in \Gamma$ of vertices connected by edges.

Steps 1 and 2 respectively carry out the process of removing order-1 spins (corresponding to single-qubit generators; we can remove these spins as this preserves the partition function up to a constant multiplicative factor)

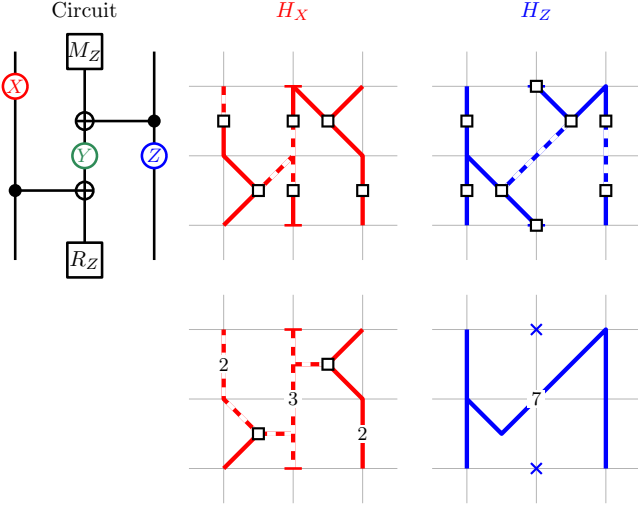


Figure 2. (Top) An example circuit for a two-qubit ZZ measurement via an ancilla qubit, with associated spin diagrams on the right, using the conventions in Fig. 1. Endcaps mark the corresponding termination of the interaction lines (open lines may join up with interactions at earlier/later times.) Errors occur in-between circuit operations; an example error realization is shown. These flip the sign of bonds on the spin model (dashed lines). Y errors flip signs on both H_X and H_Z . (Bottom) Spins with one interaction are integrated out and the interaction removed from H_X (marked by crosses). Spins with two remaining interactions are integrated out and their interactions grouped together. The combined interactions are weighted by the number of spacetime locations grouped into that interaction (unlabeled lines are weight one).

and grouping together interactions for order-2 spins. In this way, each connected component includes interactions from the unintegrated Hamiltonian that are combined together into one weighted interaction in the integrated Hamiltonian. Some connected components may still consist of only one vertex: these are interactions from the Hamiltonian that persist after integration.

Prior to integration, each interaction represents the probability of an error occurring at a spacetime location and with a Pauli flavor $\alpha = X, Z$. To preserve the partition function, the new interactions must take into account the probabilities of errors occurring at any of the spacetime locations in each of the connected components. Only the parity of the number of errors is important: by construction, an even number of errors on a connected component is gauge-equivalent to the identity. If a connected component includes x vertices labeled $\alpha = X$, and z for $\alpha = Z$, the probability that an odd total number of errors occurs across that component is

$$p_{X,Z}^{(x,z)} = \frac{1}{2} [1 - (1 - 2p_X)^x (1 - 2p_Z)^z]. \quad (24)$$

From this, we have effective coupling strength associated

with that component (cf. Appendix A 2 a)

$$K_{XZ}^{(x,z)} = \frac{1}{2} \ln \left(\frac{1 - p_{XZ}^{(x,z)}}{p_{XZ}^{(x,z)}} \right), \quad (25)$$

and effective quenched disorder distribution

$$\eta_{XZ}^{(x,z)} \sim 1 - 2\text{Bernoulli} \left(p_{XZ}^{(x,z)} \right). \quad (26)$$

Let the weight $w_{\alpha,c}$ be the number of Pauli-flavor α vertices in component c . Using these, we define the effective Hamiltonian

$$H_E = - \sum_{c \in \Gamma} K_{XZ}^{(w_{X,c}, w_{Z,c})} \eta_{XZ,c}^{(w_{X,c}, w_{Z,c})} \prod_{k \in \Xi_c} \sigma_k, \quad (27)$$

where

$$\Xi_c = \left\{ k : \left[\prod_{(\alpha, i, \tau) \in c} [\tilde{a}]_{i, \tau}, g_k \right] = -1 \right\}, \quad (28)$$

selects spins whose generators g_k anticommute with an odd number of errors in the connected component c .

If the gauge generators are all pure- X or pure- Z , each connected component contains only one Pauli flavor: Γ splits into two disjoint graphs, Γ_X and Γ_Z . The Hamiltonian also separates, $H_E = H_{X,E} + H_{Z,E}$, with $H_{\alpha,E}$ summing over only the connected components in Γ_α . In this case, we simplify notation accordingly, writing

$$p_X^{(x)} \equiv p_{XZ}^{(x,0)}, p_Z^{(z)} \equiv p_{XZ}^{(0,z)}, \quad (29)$$

and similarly for $K_X^{(x)}$ and $\eta_X^{(x)}$.

For single-vertex connected components, $p_\alpha^{(1)} = p_\alpha$ and $K_\alpha^{(1)} = K_\alpha$. As the size of a connected component increases, $p_X^{(|c|_x)} \rightarrow \frac{1}{2}$ and $K_X^{(|c|_x)} \rightarrow 0$: physically, a net odd-parity error is more likely to occur on larger components, and consequently the Hamiltonian places a smaller energy penalty on that interaction being violated. If the size of a component scales extensively with the number of spacetime qubits, in the thermodynamic limit its interaction becomes irrelevant to the free energy.

IV. REPETITION CODE

We now illustrate our framework through three simple examples, each using the 1D repetition code. First, we derive the spin models for a memory experiment and a stability experiment on the code, using a simple measurement-only brickwork circuit that elucidates the spacetime duality of these two diagnostic tools. Secondly, we compare different syndrome-extraction circuits, each mapping onto random-bond Ising models with distinct bond anisotropies. Thirdly, we examine transversal CNOT gates between repetition code patches, showing how logical operations introduce defects into these models. In

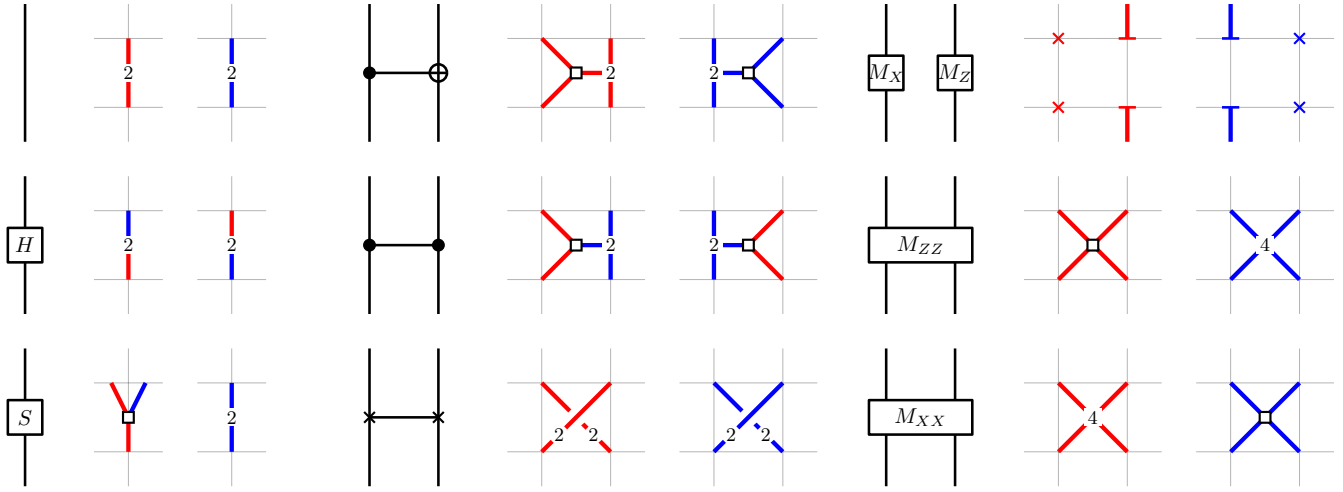


Figure 3. Common circuit elements and their spin diagrams after integrating out spins with one or two interactions. M_α are measurements of Pauli α . The SWAP gate has two weight-2 interactions for each H_α that cross over each other, swapping physical qubits. The two-qubit measurements each introduce three two-qubit gauge generators (cf. Fig. 1); when all three are integrated out, they create a weight-4 grouped interaction on all four spacetime qubits adjacent to the measurement.

these examples, we estimate maximum-likelihood decoding thresholds using Monte Carlo simulations and compare to minimum-weight perfect-matching (MWPM) decoders implemented with `Stim` [96] and `pymatching` [97]. Numerical methods are detailed in Appendix B.

The repetition code stores one logical qubit in N physical qubits, using $N - 1$ stabilizer generators of ZZ parity checks on adjacent qubits. The \bar{X} logical operator is $X_1 \otimes X_2 \otimes \dots \otimes X_N$ over all physical qubits, while the \bar{Z} logical operator is simply Z_1 (on any one physical qubit). Since there are no X stabilizers, it protects against X noise only and is essentially a classical code. We use it here as a demonstrative example for our framework, which can be readily generalized to more complicated and useful codes (cf. Sec. V).

A. Memory and stability experiments

Syndrome-extraction circuits can be used for different experimental tasks; two common diagnostic tools are the memory and stability experiments (cf. Sec. III A). Notably, the two experiments can be interpreted as spacetime duals of each other [95, 98]. As we explain in this section, this is clearly seen using their spacetime spin diagrams. The structure of these diagrams gives insight to the differences (or lack thereof) between memory and stability experimental thresholds.

We focus on the case where two-qubit ZZ measurements are the elementary building blocks. Taking into account that each qubit may undergo only one measurement at a time, the circuit takes on a brickwork spatiotemporal layout, shown in Fig. 4. (This already describes a circuit-level model in systems with native pairwise measurements [99, 100].)

a. Memory experiments. Figure 4a shows a memory experiment circuit. It begins and ends with single-qubit Z resets and measurements, respectively, creating partial detector cells along the temporal boundaries that prevent undetected timelike errors from spanning the duration of the experiment, cf. Sec. III A. Spacelike strings of errors that are gauge equivalent to a logical \bar{X} do not trigger the detectors along the spatial boundaries; these contribute towards logical equivalence classes $\bar{X}C_s\mathcal{G}$ that result in decoding failures. We construct the spin diagram by tiling components from Fig. 3. The bulk of H_X is a random bond Ising model (RBIM) on a rotated square lattice:

$$H_{X, \text{bulk}} = -K_X^{(1)} \sum_{\langle i,j \rangle} \eta_{X,\langle i,j \rangle}^{(1)} \sigma_i \sigma_j, \quad (30)$$

with $\langle i,j \rangle$ the bonds of the lattice. The open spatial boundaries produce weight-2 timelike bonds

$$-K_X^{(2)} \eta_{X,\langle i,j \rangle}^{(2)} \sigma_i \sigma_j. \quad (31)$$

Due to the qubit initialization and final readouts, on the temporal boundaries we have field terms

$$-2K_X^{(1)} \eta_{X,i}^{(1)} \sigma_i, -K_X^{(2)} \eta_{X,j}^{(2)} \sigma_j. \quad (32)$$

As there are no X -measurements, all Z errors are undetected and are gauge-equivalent to anywhere in the circuit. Consequently, all vertices in Γ_Z are connected, forming a single extensive component. H_Z is a constant, independent of the spin configuration: all $\mathbb{P}(\bar{E}) = \mathbb{P}(\bar{E}')$ where E, E' are pure- Z .

It is well-established that the repetition code subjected to measurement errors under a phenomenological noise model maps onto the square lattice RBIM [5]. Here, spin

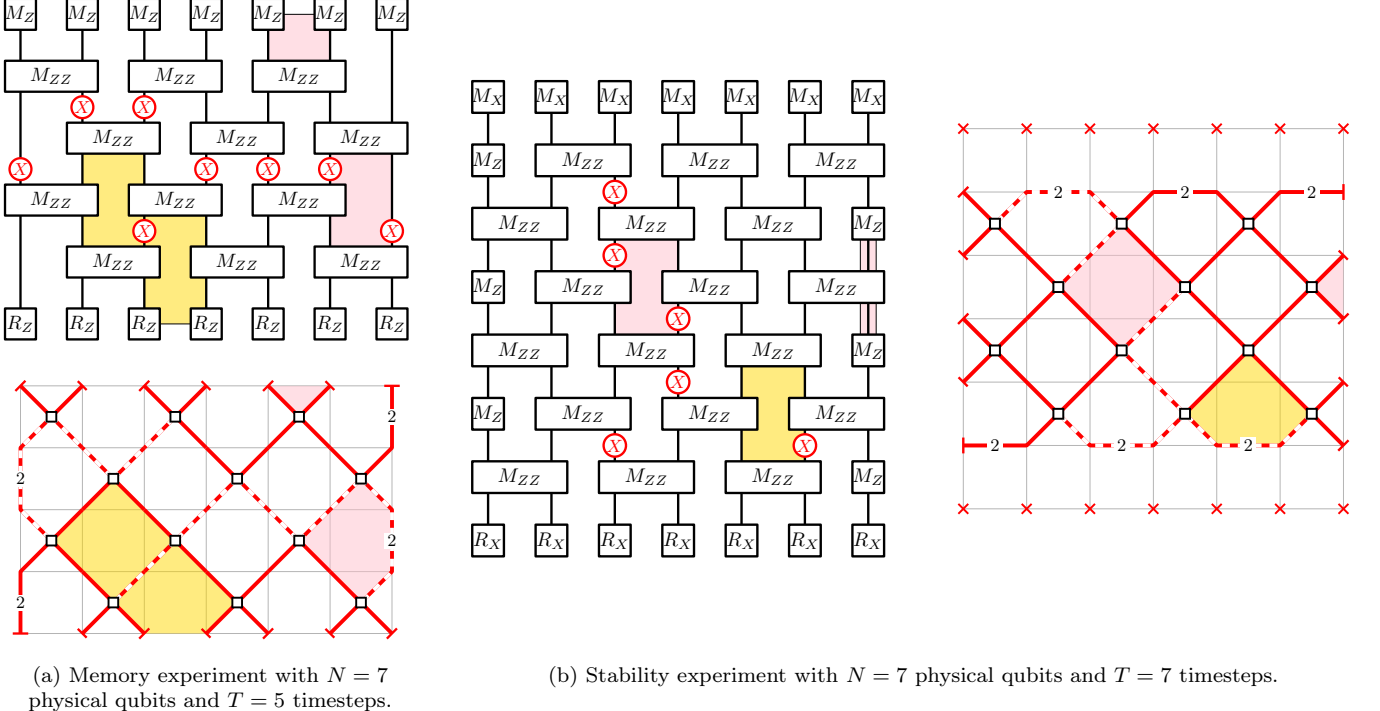


Figure 4. Measurement circuits for repetition code experiments, where errors occur in-between each circuit operation. We show representatives of error cosets that lead to decoding failures. The detector cells triggered by these errors are highlighted in yellow; some untriggered detector cells are shown in pink. Both circuits map onto a random-bond Ising model on a rotated square lattice. The errors flip the sign of bonds, indicated by dashed lines, and form a chain on the dual lattice. Detector cells form plaquettes of the lattice, and triggered detector cells host Ising vortices at the endpoints of the chains. The spatial and temporal (open) boundary conditions are interchanged between the two experiments.

diagrams have allowed us to easily derive the associated spin model for our circuit: an RBIM, but on a rotated square lattice. Unlike previous works, we have no explicit measurement errors; the non-simultaneous layering of gates (i.e., brickwork) and the repeated syndrome measurements bring about the two-dimensional structure.

b. Stability experiments. Figure 4b shows a stability experiment for the repetition code, again using only measurements. The initialization and final measurements are now in the X basis to prevent detector cells from forming on the temporal boundaries, enabling logical equivalence classes with undetected spanning timelike errors, while partial stabilizers⁸ are measured on the spatial boundaries to detect spanning spacelike errors and remove these unwanted equivalence classes from the experiment [95]. The bulk of the Hamiltonian is again a rotated RBIM. On the spatial boundaries, however, we now have field terms due to the single-qubit Z measurements truncating the interactions from each M_{ZZ} spin. On the temporal boundaries, weight-2 spatial bonds are created after re-

moving order-1 spins from each R_X and M_X , leaving the adjacent M_{ZZ} spins as order-2.

From the spin diagrams, the spacetime duality between the memory experiment and stability experiments is apparent. The error thresholds of the repetition code in a memory experiment (determined by the free energy cost of a spacelike logical operator) and in a stability experiment (from the free energy cost of an undetected spanning timelike error) should be identical. To test this, we perform numerical simulations of the circuit using the MWPM decoder. Each run a syndrome is passed to the decoder, which estimates the underlying error. The memory experiment is a success if the decoder predicts an eigenvalue of $\bar{Z} = Z_1$ (based on anticommutation with its estimated error) that is consistent with the true eigenvalue at the end of the circuit. Similarly, the stability experiment is a success if the decoder predicts the correct value for the product of stabilizer measurement outcomes $Z_1, Z_1 Z_2, Z_2 Z_3, \dots, Z_{N-1} Z_N, Z_N$.⁹ In the absence of errors, this product is always trivial (each Z_i is included twice). In Fig. 4b, for example, the true outcome would be -1 due to the X error before the final round of M_{ZZ} .

⁸ These are logical Z operators for the repetition code, hence they remove the logical degree of freedom; equivalently, they define boundary stabilizers for the spacetime code on which X -strings cannot terminate.

⁹ Qubit 1 is on the left of Fig. 4b; Z_1 and Z_N are the single-qubit M_Z on the spatial boundaries.

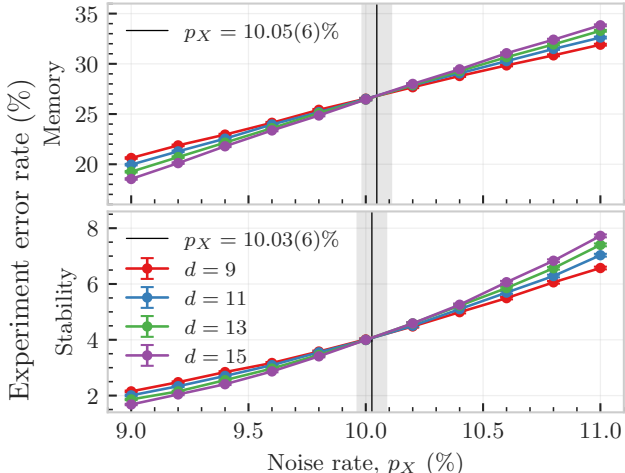


Figure 5. Error rates for memory and stability experiments corresponding to the repetition code measurement circuits in Figs. 4a and 4b respectively, using MWPM decoders with circuits of size $N = d$, $T = 2d + 1$. Both exhibit the same threshold, the noise rate p_X below which increasing d decreases the experimental error rate: approximately 10.0%.

Figure 5 shows the failure rates of these experiments at different bit-flip noise rates p_X . Vertical lines indicate the approximate location of the threshold computed via least-squares estimation in the vicinity of the crossing (cf. Appendix B 2). Both experiments, as predicted, exhibit an equal threshold of approximately 10.0%.

The ordered-disordered phase transition of a square lattice RBIM along the Nishimori line is known to occur at $p = 10.94(2)\%$ [101, 102]. Accounting for boundaries—contributing field terms and enhanced finite-size effects—it is reasonable to expect a threshold to deviate from this value. Indeed, running Monte Carlo simulations (cf. Appendix B) to compute the free energy of the spin model for the memory experiment, Fig. 6 highlights a crossing point in the logical error rate at $p = 10.77(8)\%$. MWPM decoders consider only the most-likely error rather than the error cosets and are therefore not optimal; the lower threshold of approximately $p_X = 10\%$ and consistently higher logical error rates (at $p_X = 10\%$, the MWPM exhibits a logical error rate of approximately 26% compared to the SM Monte Carlo 24 – 25%, for example) reflect this. This discrepancy in MWPM threshold from the 10.5(2)% zero-temperature critical value found in Ref. [103] may also be accounted for by finite size effects.

B. Circuit compilations

The stabilizers of a QEC code can be compiled into syndrome-extraction circuits in a variety of ways. The choice of implementation may be influenced by factors

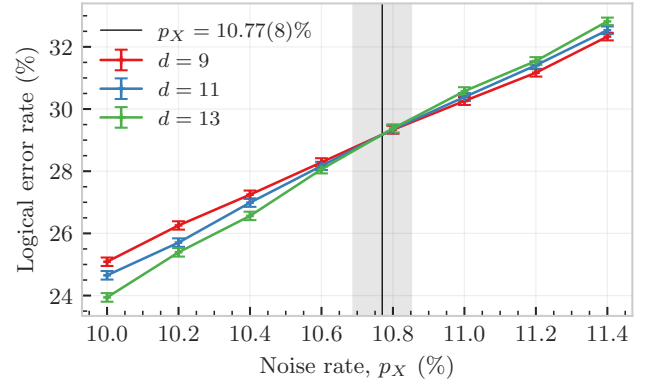


Figure 6. Monte Carlo simulations of the logical error rate from free-energy decoding of the repetition code memory experiment from Fig. 4a with $N = d$, $T = 2d + 1$. A crossing occurs at $p_X = 10.77(8)\%$, higher than the 10.05(6)% from MWPM decoding in Fig. 5.

such as the native hardware-efficient gate set or a need to tolerate fabrication defects [74–76, 79]. In this section, we demonstrate how different syndrome-extraction circuits for the repetition code can be mapped onto spin diagrams with distinct bond anisotropies. We compare these models to offer insight into the differing performance of these circuits.

a. Standard ancilla circuit. Figure 7 shows detector cells for a compiled syndrome extraction circuit for the repetition code, performing ZZ measurements using ancilla qubits and $CNOT$ operations (cf. Fig. 2). Unlike the memory and stability experiment circuits, measurements of all stabilizers are performed in parallel, while the $CNOT$ s introduce complexities to the spread of errors (e.g., hook errors). Applying the spins for $CNOT$ s from Fig. 3, each weight-2 interaction combines with an additional weight-2 interaction to form a single one of weight-3, and we get the spin diagram in Fig. 7a. Re-arranging the bonds (cf. Fig. 7c) reveals a random-bond Ising model on a sheared honeycomb lattice, with anisotropic bond strengths (with weights 1, 3, 3). The bulk Hamiltonian is

$$H_X = - \sum_{\langle i,j \rangle} K_X^{(w_{\langle i,j \rangle})} \eta_{X,\langle i,j \rangle}^{(w_{\langle i,j \rangle})} \sigma_i \sigma_j, \quad (33)$$

where $w_{\langle i,j \rangle} \in \{1, 3, 3\}$ depends on the bond. The shearing is necessary to preserve the timelike direction of the lattice; far from any boundaries, however, the behavior should be equivalent to an un-sheared honeycomb lattice. The anisotropy and boundary conditions place this SM model in a different universality class from the typical honeycomb RBIM; its critical values will be different and we will determine them numerically.

b. Wiggling ancilla circuit. McEwen *et al.* [74] introduced an alternate, dynamic syndrome-extraction circuit for the repetition code that exchanges the roles of data and ancilla qubits, producing a “wiggling” pattern

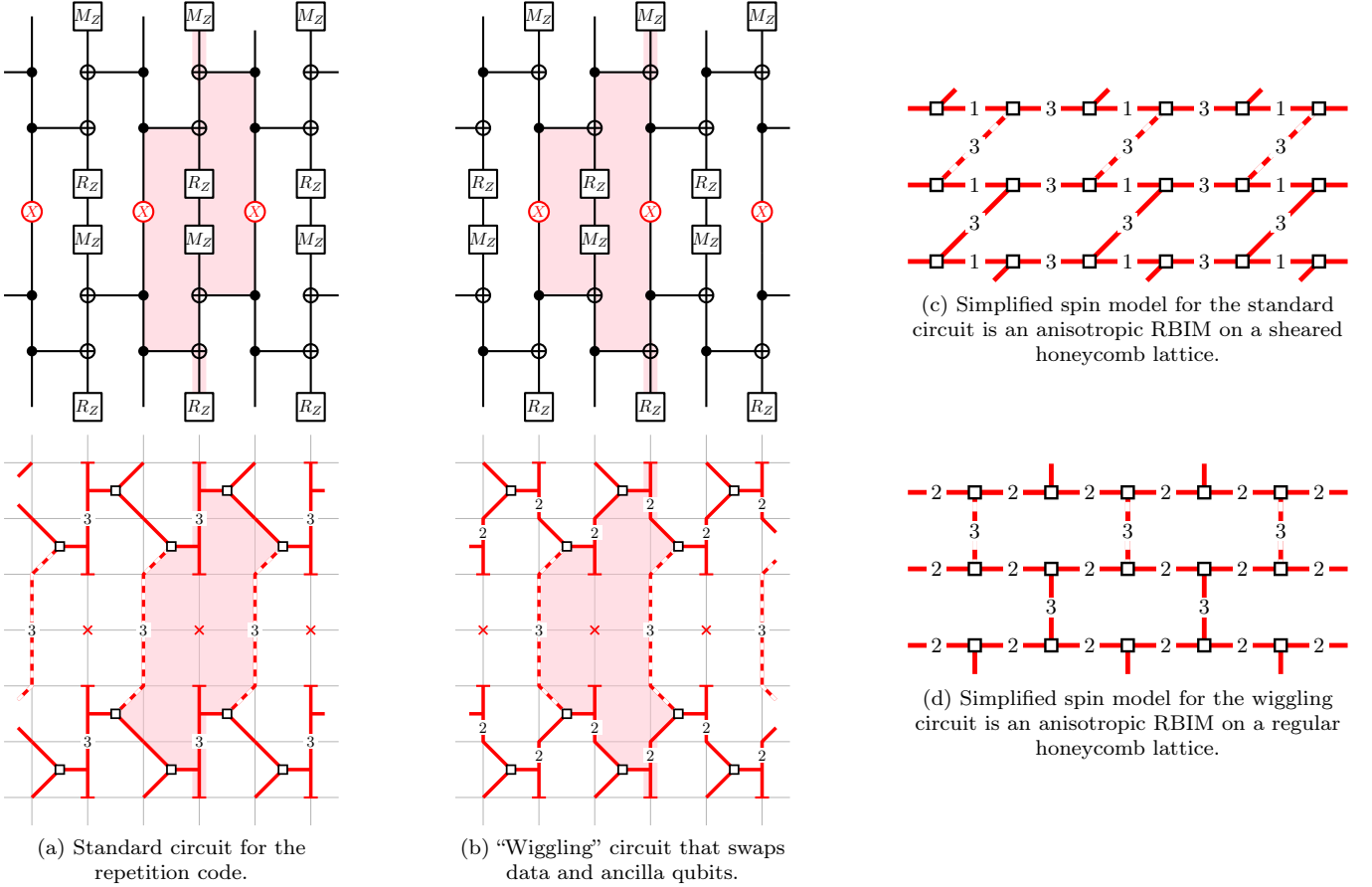


Figure 7. Different syndrome-extraction circuits for the repetition code. Spin diagrams have degree-2 spins integrated out and replaced with weighted interactions (labeled; 1 if omitted). A cross indicates a removed interaction from a degree-1 spin. Detector cells (one highlighted in pink) map onto plaquettes of the spin lattice; triggered detectors (none shown) again host Ising vortices. Part of a logical \bar{X} error is shown on the circuit; dashed bonds of the spin model show those flipped by the error. Re-arranging bonds to simplify reveals an equivalence to anisotropic random-bond Ising models on honeycomb lattices.

in the detector cells. Figure 7b shows this circuit and the corresponding spin diagrams. As with the regular circuit, the simplified model (cf. Fig. 7d) is a random bond Ising model, this time on an un-sheared honeycomb lattice with anisotropic weights $w_{\langle i,j \rangle} \in \{2, 2, 3\}$. In the bulk of the model, the shear does not affect local interactions—the difference in memory-experiment threshold between these models should be solely due to the differing anisotropy.

To understand the difference in decoding performance of these two circuits, consider the free energy cost of inserting a spatial logical operator. One representative of this logical operator is the product of X over all qubits in-between each measurement and reset, indicated by the circular errors and dashed bonds in Fig. 7. Starting from a ground state with $\eta_{X,\langle i,j \rangle} = 1$ and $\sigma_i = 1$ for both models, applying the logical error flips vertical weight-3 bonds. The energy cost is identical for both circuits. However, we need to account for the energies of gauge-equivalent errors when computing free-energy differences. Flipping a spin attached to the affected bonds (i.e., in-

cluding a gauge operator to deform the logical error) changes energy by $\Delta\mathcal{E}_{\text{standard}} = 2K_X^{(1)}$ in the standard circuit, and $\Delta\mathcal{E}_{\text{wiggling}} = 4K_X^{(2)} - 2K_X^{(3)}$ in the wiggling circuit. Taking the low-error limit of Eq. (25), one can show that

$$\lim_{p_X \rightarrow 0} \left(K_X^{(x)} - K_X^{(x')} \right) = \frac{1}{2} \ln \left(\frac{x'}{x} \right), \quad (34)$$

and thus

$$\lim_{p_X \rightarrow 0} (\Delta\mathcal{E}_{\text{standard}} - \Delta\mathcal{E}_{\text{wiggling}}) = \ln \left(\frac{4}{3} \right). \quad (35)$$

From this, we can infer that domain walls separating regions of flipped spins cost more energy to move in the standard circuit, leading to larger free-energy barriers. An ML decoder of the standard circuit will more accurately discern the correct logical class. This suggests lower sub-threshold ML logical error rates for the standard circuit; the larger energetic barriers also suggest a higher error threshold than for the wiggling circuit.

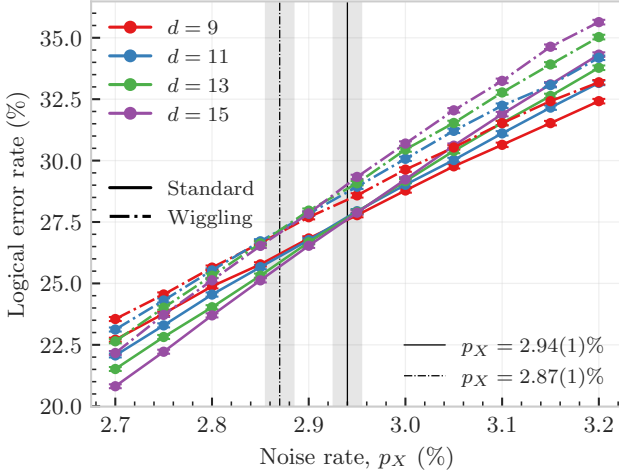


Figure 8. MWPM error rates for memory experiments of the standard (solid line) and wiggling (dot-dashed line) repetition code circuits with $N = 2d-1$, $T = 4d-1$. The wiggling circuit has a lower threshold at $2.87(1)\%$ compared to $2.94(1)\%$ for the standard circuit.

The suppressed fluctuation of errors strings for the standard circuit also suggest that its MWPM decoding (picking the minimum-energy string) will be more accurate at low p_X than for the wiggling circuit (resulting in lower logical error rate). We also expect the MWPM thresholds to reflect the ML threshold differences: a higher threshold for the standard circuit.

We performed simulations of MWPM decoding for a memory experiment with both circuits. We simulated a circuit depth of $T = 4d-1$; below that, the code displayed above-threshold behavior with logical error rate increasing with distances. We plot the results of the memory experiment in Fig. 8: the standard circuit consistently achieves lower logical error rates, as we expected based on our spin models. The standard circuit has a MWPM threshold of approximately $2.94(1)\%$, while the wiggling circuit has a lower threshold of $2.87(1)\%$. This is also consistent with our expectations. Running Monte Carlo simulations of the spin models and estimating the ML decoding error rates, Fig. 9 shows a threshold of $2.98(1)\%$ for the standard circuit, slightly exceeding the MWPM threshold. The logical error rates themselves are also lower for the ML decoder, achieving a rate of 19% at $p_X = 2.7\%$ and $d = 11$, compared to 22% for the MWPM decoder, for example.

As this circuit compilation comparison illustrates, our framework serves both as a source of intuition for performance differences, as well as a tool for quantitative comparisons to ML decoders.

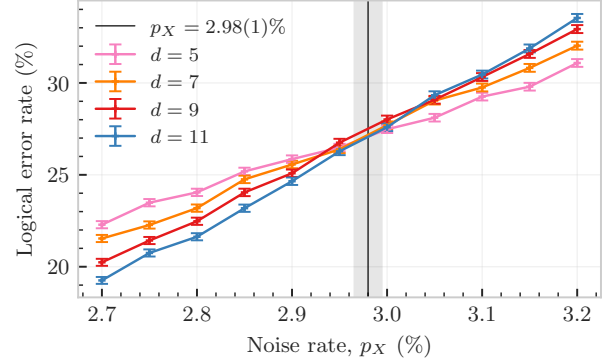


Figure 9. Monte Carlo simulations of the logical error rate for a standard repetition code circuit with $N = 2d-1$, $T = 4d-1$. A threshold of $2.98(1)\%$ exceeds the MWPM threshold of $2.94(1)\%$ from Fig. 8.

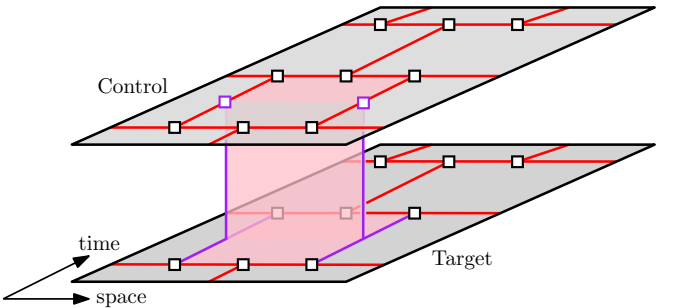


Figure 10. A transversal CNOT between two repetition codes modifies the H_X spin diagram of the system (here shown for syndrome extraction circuits as in Fig. 7) by introducing a row of additional spins on the control logical qubit that couple with pairs of spins on the target (highlighted in purple). Detector cells at the inter-code couplings now span both code patches (such a cell shown in pink).

C. Logical circuits

Our dynamical spin model framework also naturally encompasses logical circuits—the QEC of quantum computations. For example, a logical CNOT gate between two repetition codes running syndrome extraction circuits can be implemented transversally via CNOT gates on each corresponding data qubit in the two code patches. Compared to a circuit with idling logical qubits (cf. Fig. 7), each introduced CNOT modifies the local structure in two ways (cf. Fig. 10): on each control qubit, H_X is modified to include an additional spin; and this is coupled to H_X of the target logical qubit through a three-spin interaction with a pair of target spins. Acting across all data qubits, a transversal CNOT introduces a defect line, coupling spins between the two code patches. If a spin on the control patch involved in this coupling flips to $\sigma_{\text{control}} = -1$, this effectively inverts the sign of the interaction on the tar-

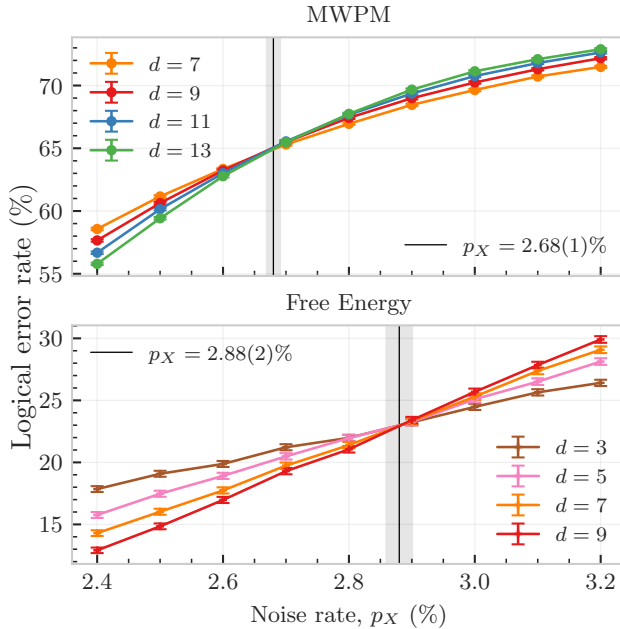


Figure 11. Logical error rates for a pair of repetition codes with standard syndrome extraction circuits subjected to a transversal CNOT gate, using both a MWPM decoder and free energy calculations of the spin model, with $N = 4d - 2$, $T = 16d - 1$ for MWPM and $T = 4d - 1$ for the free energy (ML) decoder. The MWPM decoder required a larger circuit depth to observe a threshold; the error rates between these two decoders are therefore not directly comparable. The ML threshold is significantly higher than the MWPM threshold.

get, converting ferromagnetic to antiferromagnetic bonds (and vice-versa). Increasing the error rate (i.e., weakening the interaction strengths) in the control patch promotes flipping the spins associated with the transversal CNOT, and this increases the disorder on the target patch. We thus expect the overall logical error rate, at a given p_X , to be larger than for two decoupled patches—and the error threshold to be lower. This spin-coupled behavior between the two code patches encodes the effect of hook errors on the circuit—a single-qubit error on the control qubit is gauge-equivalent to a two-qubit error on both qubits after the CNOT.

We expect the threshold of the model to decrease when subjected to transversal CNOT gates. Figure 11 shows the estimated logical error rates for the standard syndrome extraction circuit, using both MWPM decoding and Monte Carlo simulations of the free energy. A logical error is deemed as occurring if the decoder fails to predict the correct error coset for either of the two code patches. Simulations of the MWPM decoder were unable to produce thresholds for circuit depths smaller than $T = 16d - 1$, and it was computationally infeasible to simulate spin models for these larger system sizes—for this reason, the logical error rates in Fig. 11 are not di-

rectly comparable. For comparison, simulations of the MWPM decoder at $T = 4d - 1$ (not plotted) consistent with the ML simulations produced a logical error rate around 38% for $d = 9$ and $p_X = 2.9\%$, which is notably larger than the 23% of the ML decoder. Thresholds, on the other hand, are properties of the circuit and noise model, and (up to finite-size effects) remain comparable at different circuit depths. In Fig. 11, we observe an ML threshold at 2.88(2)%—lower than the 2.98(1)% of the single code patch. This agrees with the prediction based on the discussion of the defect line introduced by the transversal CNOT. For MWPM, we observe a threshold at 2.68(1)%, well below the 2.94(1)% threshold for a single patch. Whereas the difference between ML and MWPM thresholds for the circuits in Sec. IV B was around only 0.03 percentage points, the larger discrepancy seen here may be accounted for by the MWPM algorithm, which requires that each single-qubit error flips at most two detectors (a “graphlike” detector-error model). An X error on a control qubit after the CNOT, however, flips four detectors: two from its own code patch (as usual) and two additional from the target code patch (that now extend across both patches due to the CNOT); an example detector that spans both code patches is shown in Fig. 11. While the MWPM decoder can overcome this by decomposing such errors into products of graphlike errors, doing so introduces suboptimality [97]. The same considerations apply for the notable gap between the single-patch and CNOT MWPM thresholds.

Instead of one transversal CNOT occurring at the midpoint of the repetition code circuit, we may instead consider the effect of transversal CNOTs occurring within each detector cell of a circuit. Performing numerical simulations (not plotted), the MWPM decoder is now unable to reproduce a threshold, even at extended circuit depths, as an extensive number of non-graphlike errors exist across the detector error model. The ML decoder, on the other hand, sees a threshold near $p_X = 2.70(5)\%$ —a decrease from the 2.88(2)% in Fig. 11. Despite the presence of defects introduced by the transversal CNOTs to every unit cell of the spin model, there nevertheless persists an error-correcting phase at non-zero p_X .

The discussions in this section naturally extend to other codes with transversal CNOTs, different transversal logic gates, and even lattice surgery or code-switching protocols, for example. Spin models of logical circuits thus allow us to probe the limits of decoding techniques, considering the error-correcting behavior of quantum circuits, rather than merely quantum memories.

V. TORIC CODE

The repetition code, detecting only X errors, is an instructive albeit simplistic example of the usefulness of SM mappings. Moving to codes that detect both X and Z errors, our mappings allow us to model and investigate different aspects of its error-correcting behavior, such as

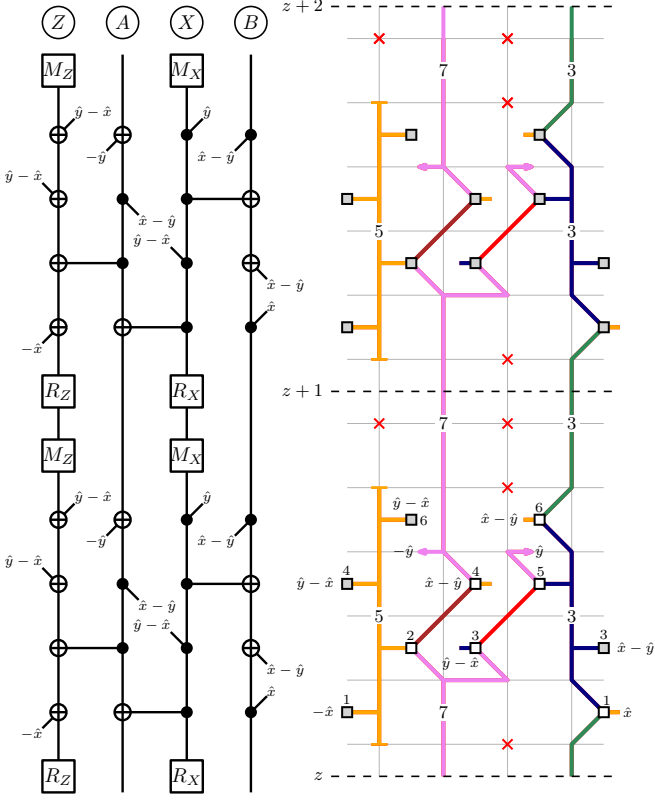


Figure 12. Part of a standard syndrome-extraction circuit for the toric code, creating both an X -error and Z -error detector cell. The code is split into a unit cell with four qubits labeled Z , A , X and B , as sketched in Fig. 13. Unit cells are indexed by lattice directions (x, y, z) (with z timelike; separated by dashed lines in the spin diagram). Partially shown CNOTs couple to other unit cells in the directions indicated. The spin diagram for H_X shows one unit cell with six spins (white squares and labeled 1-6; spins from adjacent sites are gray) and six bonds [colored to reference Eq. (36)]. Arrows show a bond connecting to another unit cell.

the effects of different circuit compilations or of logical operations. We also observe richer structure in the form of local \mathbb{Z}_2 gauge symmetries, which emerge from the spacetime geometry of detector cells. We demonstrate this now using the toric code.

A. Circuit compilations

The toric code encodes two logical qubits on a periodic 2D lattice using weight-four X and Z stabilizers on alternating plaquettes [3, 5, 6]. Figure 12 shows a standard syndrome-extraction circuit using ancilla qubits [5, 74]. The corresponding SM model is 3D and has more complex spin geometries than our prior examples. A unit cell for H_X is sketched in Fig. 12 and Fig. 13 by applying the elementary spin components from Fig. 3 to the circuit. (The spacetime code is CSS and H_Z has an equivalent

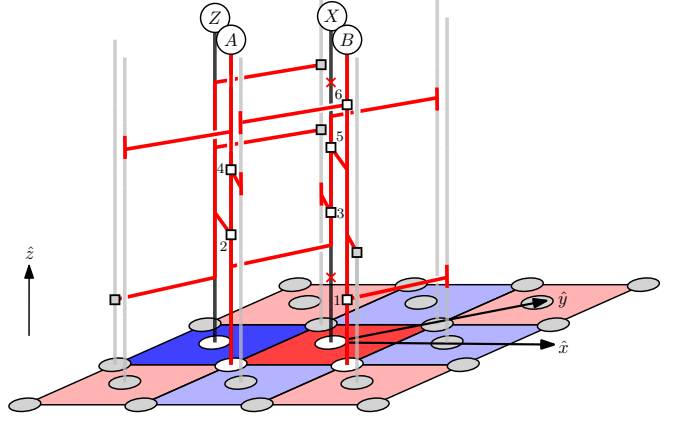


Figure 13. A 3D unit cell for the toric code H_X , based on the syndrome extraction circuit in Fig. 12. Each unit cell is half a detector cell, and has 4 physical qubits (labeled Z , A , X , and B), 6 spins (labeled $\sigma_{i,x,y,z}$ for $i = 1, \dots, 6$), and 6 bonds (signs labeled as $\eta_{j,x,y,z}^{(w)}$ for $j = 1, \dots, 6$).¹⁰ Writing down the interactions from the model, we have a bulk Hamiltonian

$$\begin{aligned}
 H_X = & - \sum_{x,y,z} \left(K^{(1)} \eta_{1,x,y,z}^{(1)} \sigma_{2,x,y,z} \sigma_{4,x,y,z} \right. \\
 & + K^{(1)} \eta_{2,x,y,z}^{(1)} \sigma_{3,x,y,z} \sigma_{5,x,y,z} \\
 & + K^{(3)} \eta_{3,x,y,z}^{(3)} \sigma_{1,x,y,z} \sigma_{3,x+1,y-1,z} \sigma_{5,x,y,z} \sigma_{6,x,y,z} \\
 & + K^{(3)} \eta_{4,x,y,z}^{(3)} \sigma_{1,x,y,z} \sigma_{6,x,y,z-1} \\
 & + K^{(5)} \eta_{5,x,y,z}^{(5)} \sigma_{1,x-1,y,z} \sigma_{2,x,y,z} \sigma_{4,x-1,y+1,z} \sigma_{6,x-1,y+1,z} \\
 & \left. + K^{(7)} \eta_{6,x,y,z}^{(7)} \sigma_{2,x,y,z} \sigma_{3,x,y,z} \sigma_{4,x,y,z-1} \sigma_{5,x,y-1,z-1} \right) \quad (36)
 \end{aligned}$$

with colors matching Fig. 12.¹¹ Compared to the repetition code, this is a more complex Ising model, with two or four spins per interaction, and weights up to 7.

As we did with the repetition code, we can also consider alternate syndrome-extraction circuits. The wiggling toric code circuit from McEwen *et al.* [74] is shown in Fig. 14. Because ancilla and data qubits are interchanged in the circuit, the second half of each detector cell circuit is the reverse of the first half. The spin model unit cell encompasses both halves and now extends twice as long in time and includes 12 spins and 12 bonds. These

¹⁰ A slightly unusual choice of lattice directions is observed to respect the checkerboard pattern of the plaquettes; to keep \hat{x} and \hat{y} orthogonal we would need to extend to a 12-spin unit cell.

¹¹ X subscripts on K and η are omitted for clarity.

form the Hamiltonian

$$\begin{aligned}
H_X = - \sum_{x,y,z} & \left(K^{(1)} \eta_{1,x,y,z}^{(1)} \sigma_{2,x,y,z} \sigma_{4,x,y,z} \right. \\
& + K^{(1)} \eta_{7,x,y,z}^{(1)} \sigma_{8,x,y,z} \sigma_{4,x,y,z} \\
& + K^{(1)} \eta_{2,x,y,z}^{(1)} \sigma_{3,x,y,z} \sigma_{5,x,y,z} \\
& + K^{(1)} \eta_{8,x,y,z}^{(1)} \sigma_{9,x,y,z} \sigma_{11,x,y,z} \\
& + K^{(4)} \eta_{3,x,y,z}^{(4)} \sigma_{1,x,y,z} \sigma_{2,x,y,z} \sigma_{4,x,y-1,z} \sigma_{6,x+1,y-1,z} \\
& + K^{(4)} \eta_{9,x,y,z}^{(4)} \sigma_{7,x+1,y-1,z} \sigma_{8,x,y-1,z} \sigma_{10,x,y,z} \sigma_{12,x,y,z} \\
& + K^{(3)} \eta_{4,x,y,z}^{(3)} \sigma_{1,x,y,z} \sigma_{12,x,y,z-12} \\
& + K^{(3)} \eta_{10,x,y,z}^{(3)} \sigma_{6,x,y,z} \sigma_{7,x,y,z} \\
& + K^{(4)} \eta_{5,x,y,z}^{(4)} \sigma_{1,x,y,z} \sigma_{3,x-1,y+1,z} \sigma_{5,x-1,y,z} \sigma_{6,x,y,z} \\
& + K^{(4)} \eta_{11,x,y,z}^{(4)} \sigma_{7,x,y,z} \sigma_{9,x-1,y,z} \sigma_{11,x-1,y+1,z} \sigma_{12,x,y,z} \\
& + K^{(7)} \eta_{6,x,y,z}^{(7)} \sigma_{2,x,y,z} \sigma_{3,x,y,z} \sigma_{10,x,y,z-1} \sigma_{11,x+1,y-1,z-1} \\
& \left. + K^{(7)} \eta_{12,x,y,z}^{(7)} \sigma_{4,x,y,z} \sigma_{5,x-1,y+1,z} \sigma_{8,x,y,z} \sigma_{9,x-1,y+1,z} \right) \quad (37)
\end{aligned}$$

As with the repetition code, we can form a qualitative understanding of the differences in ML decoding by examining the free energy cost of inserting a spatial logical operator. One representation of the \bar{X} logical is X over all qubits in-between each measurement and reset. On both circuits' spin diagrams, this flips $\eta_{4,x,y,z}^{(3)}$ and $\eta_{6,x,y,z}^{(7)}$ along all x at some y, z . For a ground state of all $\eta = 1$ and $\sigma = 1$, the energy cost is identical for both circuits. We then consider gauge-equivalent errors. Flipping spin $\sigma_{1,x,y,z}$ deforms the logical error by a gauge operator,¹² and changes energy by $\Delta E_{\text{standard}} = 2K^{(5)}$ in the standard circuit and $\Delta E_{\text{wiggling}} = 4K^{(4)} - 2K^{(3)}$ in the wiggling circuit. Using Eq. (34), in the low-noise limit we get

$$\lim_{p_X \rightarrow 0} (\Delta E_{\text{standard}} - \Delta E_{\text{wiggling}}) = \ln \left(\frac{16}{15} \right). \quad (38)$$

We obtain the same result as with the repetition code: the wiggling circuit assigns a lower energy penalty to fluctuations of the logical error strings compared to the standard circuit, and hence ML and MWPM decoders for the standard circuit should exhibit (slightly) lower logical error rates and higher thresholds.

To verify this, we simulate MWPM decoding of toric code memory experiments. Figure. 15 shows a threshold of 0.3655(3)% for the standard circuit, higher than the 0.3628(3)% for the wiggling circuit, in agreement with our energy analysis. Logical error rates for the standard

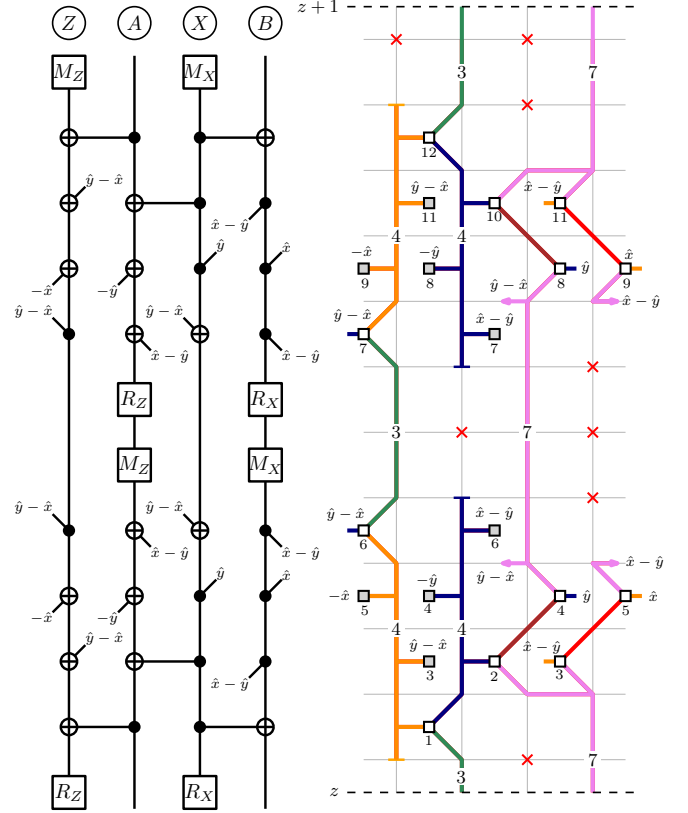


Figure 14. Part of a wiggling syndrome-extraction circuit for the toric code, along with its spin diagram for H_X . Each unit cell again contains four physical qubits Z, A, X and B (cf. Fig. 13), but the timelike direction is twice as long to accommodate the wiggling structure. There are 12 spins (white squared; spins from adjacent sites are gray) per unit cell and 12 bonds [colored to reference Eq. (37), and highlighting the symmetric structure of the unit cell].

circuit are also consistently lower (for the same distance and noise rate) compared with the wiggling circuit.

These thresholds appear to be considerably lower than the 2.93(2)% threshold for MWPM decoding of a toric code with a phenomenological noise model of bit-flip and measurement errors [104]. Our circuit-level noise models are not directly comparable to phenomenological noise models, however, as every detector cell in our circuit supports 44 spacetime locations where an error can trigger it, compared to six in the phenomenological. A rough comparison can be drawn by considering the threshold as an effective noise rate per detector cell (the probability of a detector being triggered) using Eq. (24): $\frac{1}{2}[1 - (1 - 2 \times 0.003655)^{44}] = 13.8\%$ for our results, compared to $\frac{1}{2}[1 - (1 - 2 \times 0.0293)^6] = 15.2\%$ for the phenomenological model. These results are more consistent, with a lower threshold potentially due to the increased complexities of error propagation through the circuit's CNOTs. For further comparison, under circuit-level depolarizing noise the toric code has a MWPM threshold

¹² This is the lowest-energy deformation, and therefore the most likely at low temperature (low noise).

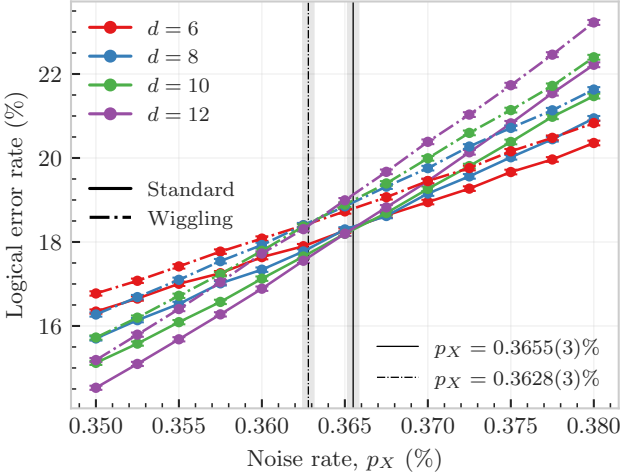


Figure 15. MWPM logical error rates for the standard (solid line) and wiggling (dashed) toric code syndrome-extraction circuits, with $N = 2d^2$, $T = 12d$. As predicted from interaction-weight arguments, the wiggling circuit has a slightly lower threshold and higher error rate.

of 0.60% [105]. Depolarizing noise often results in higher thresholds due to induced correlations; a toric code with a phenomenological bit-flip noise channel without measurement errors gives a 10.94(2)% ML threshold [101, 102], compared to 18.9(3)% for depolarizing noise [13, 106].

B. Gauge symmetries

Each X -flavored detector cell (corresponding to an X stabilizer in the spacetime code, and covering two unit cells in the standard circuit's H_X) introduces a local constraint: the product of all X -flavored gauge generators within a single detector cell equals the identity. In the spin language, this means H_X is invariant under local \mathbb{Z}_2 gauge symmetries. For the standard toric code [Eq. (36)], these are

$$\phi_{x,y,z} = \text{flip all } \{\sigma_{2,x,y,z}, \sigma_{3,x,yz}, \sigma_{4,x,y,z}, \sigma_{5,x,y,z}, \sigma_{6,x,y,z}, \sigma_{6,x-1,y+1,z}, \sigma_{1,x,y,z+1}, \sigma_{1,x-1,y+1,z+1}, \sigma_{2,x,y+1,z+1}, \sigma_{3,x,y,z+1}, \sigma_{4,x,y+1,z+1}, \sigma_{5,x,y,z+1}\} \quad (39)$$

These symmetries arise generically in any model with an overcomplete set of chosen gauge generators g_k . For example, around an M_{ZZ} measurement (cf. Fig. 1), including all four generators $g_1 = [Z]_{i,t-0.5}[Z]_{i,t+0.5}$, $g_2 = [Z]_{j,t-0.5}[Z]_{j,t+0.5}$, $g_3 = [ZZ]_{\{i,j\},t-0.5}$ and $g_4 = [ZZ]_{\{i,j\},t+0.5}$ creates a redundancy with $g_1g_2g_3g_4 = I$. This introduces the local gauge symmetry $\phi = \text{flip all } \{\sigma_1, \sigma_2, \sigma_3, \sigma_4\}$. In this example, the redundancy can be easily avoided (the gauge symmetry fixed) by including only three of these g_k (as we did in Fig. 1). In detector cells, however, the involved spins may span sev-

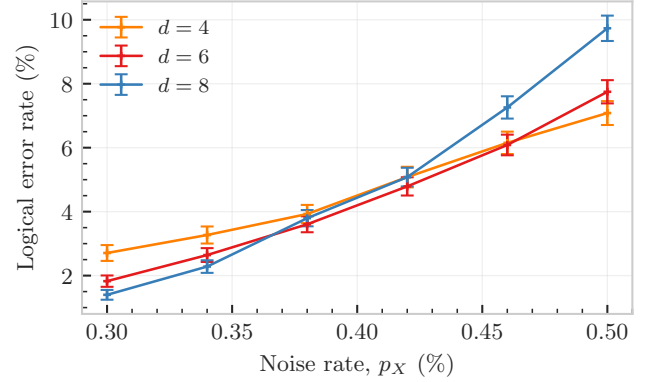


Figure 16. Estimates of the ML logical error rates for the toric code memory experiment with $N = 2d^2$, $T = 3d$ using Monte Carlo SM simulations. A rough threshold is observed in the regime of 0.35%-0.45%.

eral unit cells and be included in other overcomplete sets; the dependency is not generically fixable without careful examination of the model. Removing a spin may also obfuscate the relationship between gauge-equivalent error strings. For example, gauge-fixing $\phi_{x,y,z}$ by removing $\sigma_{2,x,y,z}$ hides that errors affecting interactions 1, 5, and 6 are related via the gauge group.

Gauge symmetries have practical implications for the treatment of the spin models. Gauge-invariant quantities—such as Wilson loops formed by products of spins around closed paths—correspond to observables relevant for determining phases of matter. In the toric code and other topological codes, appropriate Wilson loops may be formed by considering the bonds affected when logical operators are translated in space and time; the complicated bond interactions in our SM model, however, obfuscate the geometric significance of such objects [Eq. (36) and Eq. (37) are not the simple random plaque-gauge theories of phenomenological noise models [5]].

These gauge symmetries also constrain which Monte Carlo algorithms are efficient. Standard single-spin Metropolis updates respect the gauge symmetry but can suffer from critical slowing down near the phase transition, as they cannot efficiently sample between gauge-equivalent configurations separated by large energy barriers—an important aspect for accurately determining thermodynamic expectations that require averages over the entire configuration space. Gauge fixing removes the local gauge-equivalent spin configurations from the simulation landscape, but does not eliminate these energy barriers. Simulations of the spin model that perform single-spin updates would encounter artificial inefficiencies when attempting to propagate errors around this removed spin. Cluster algorithms that respect the gauge structure, or algorithms suited for exploring complex energy landscapes such as population annealing, may offer improved sampling performances.

Using Monte Carlo simulations, we estimate the error rates of an ML decoder for the standard toric code syndrome-extraction circuit; compared to the repetition code simulations, the higher dimensionality and gauge symmetries create a rougher energy landscape and precise determination of the threshold is computationally difficult. Increased compute power, as well as cluster update algorithms tailored to the local symmetries of Eq. (39), for example, may allow one to observe higher-precision results. Nevertheless, Fig. 16 shows an approximate threshold consistent with the MWPM result. Unlike the logical circuit from Sec. IV C, the error model produces only graphlike errors in this circuit and it is expected that MWPM performs near-optimally. The system sizes able to be simulated require that we use a circuit depth $T = 3d$, compared to the $T = 12d$ used in Fig. 15. Running MWPM decoding using $T = 3d$ (not plotted) produces logical error rates consistent (within error bars) with the ML decoder.

C. Logical circuits

We can also consider the effect that logical operations have on the spin models for the toric code. As with the repetition code, a transversal CNOT on all the data qubits of the toric code is a logical CNOT operation. The effect on the spin diagram is qualitatively equivalent to that observed with the toric code: Applied to the standard or wiggling circuits, the CNOT modifies the **weight-3** and **weight-7** interactions that connect two unit cells in the z direction. On the control logical qubit, these interactions would be replaced by two interactions, joined by an additional spin; on the code patch for the target logical qubit, these interactions would now involve **three** (**five**) spins, instead of their usual **two** (**four**) for an idling logical qubit. The additional spin and modified interaction couple together the spin models for the two logical qubits and promote increased disorder at a given noise rate p_X . The detector cells are also modified, with the X -error-detecting cell on the target code patch now including support on the control code patch, and the Z -error-detecting cell on the control code patch now including support on the target code patch. These modified detector cells result in non-graphlike errors, where single-qubit errors on the data qubits after the logical CNOT trigger four detector cells. The effect of the logical operation is therefore to decrease the efficiency of decoding, expected to result in higher logical error rates and lower thresholds, as was seen with the repetition code. We leave explicit Monte Carlo simulations of these models to future works.

VI. CONCLUSION

In this work, we established a general framework for mapping stabilizer circuits onto classical statistical mechanics models. Our approach leverages the spacetime

code representation of circuits, where the $(d+1)$ D circuit becomes a subsystem code in $(d+1)$ spatial dimensions. The probability of any logical error class becomes the partition function of a classical spin Hamiltonian, with gauge operators of the spacetime code corresponding to spin degrees of freedom. This mapping applies to arbitrary noise channels and can be constructed using a spin-diagrams, a graphical language that allows the modular construction of the SM Hamiltonian directly from the circuit elements, and which we described in detail for independent circuit-level X - Z noise.

The spin diagram formalism offers both conceptual clarity and practical utility. Each circuit element—idle wires, CNOTs, measurements, resets—contributes a standard building block of spins and interactions. Composing these blocks produces the full SM Hamiltonian without requiring the explicit computation of gauge generators or their commutation relations. These diagrams can be simplified by integrating out low-degree spins, grouping gauge-equivalent errors into weighted interactions while preserving the partition function ratios that determine the phases of the system (error-correcting or non-correcting) and hence maximum-likelihood decoding. The resulting models often take the form of generalized random-bond Ising models, connecting the rich phenomenology of disordered classical systems to the decodability of stabilizer circuits.

Our examples in Sections IV and V illustrate the capabilities of this framework. For the repetition code, we showed that memory and stability experiments map onto spacetime-dual random-bond Ising models on rotated square lattices, providing a clear geometric interpretation of why their thresholds coincide. Different syndrome-extraction circuits, such as a standard ancilla circuit and the wiggling circuit of McEwen *et al.* [74], produce honeycomb lattice models with distinct bond anisotropies. By analyzing the free-energy cost of logical operators in these models, we explained why the standard circuit achieves a slightly higher threshold and lower logical error rates, and confirmed these with MWPM simulations. These results already illustrate how SM models can provide an analytical handle for comparing circuit compilations.

Logical operations also fit naturally within our framework. For example, for the repetition code, we showed how transversal CNOT gates between two code patches introduce defect lines into the SM model, coupling spins across the two lattices and creating higher-order interactions. Monte Carlo simulations revealed that while a single transversal CNOT has minimal impact on the threshold, repeated applications—one per detector cell—reduce the threshold from 2.88(2)% to 2.70(5)%. Crucially, an error-correcting phase persists also with these defects—QEC can succeed even when considering evolving logical circuits, and not just static memories—which we not only confirm but also establish its ultimate (i.e., maximum-likelihood decoding) boundaries.

We also showed how local \mathbb{Z}_2 gauge symmetries arise from the spacetime structure of detector cells. Each X -

flavor detector cell introduces a constraint that renders the Hamiltonian invariant under simultaneous flips of all associated spins. These gauge symmetries connect circuit-level decoding to lattice gauge theory, suggesting that the spin models for topological codes are not merely random-bond Ising models but classical lattice gauge theories with gauge-invariant observables analogous to Wilson loops. This has practical implications for Monte Carlo simulations, where gauge-fixing or gauge-respecting algorithms may offer improved sampling efficiency near criticality or at low temperatures (i.e., low physical error rates).

Our framework opens several avenues for future research. An immediate next direction concerns dynamical codes [50, 51, 61–71], such as Floquet codes [39–42, 107–118] or dynamic automorphism codes [45, 47], both in platforms with native two-qubit measurements [99, 100], and in other systems where one can again compare distinct circuit compilations.

For these and further problems, one can leverage the systematic and modular nature of spin diagrams which makes them amenable to automation: given a circuit description, one could algorithmically generate the corresponding Hamiltonian and estimate thresholds via Monte Carlo methods. This would complement existing approaches for comparisons of circuit compilations, gate orderings, or scheduling strategies for a given code. It may be fruitful to also consider other circuits, such as different compilations of the surface code syndrome-extraction circuit, surface code transversal logic gates or lattice surgery, magic state factories, or code-switching architectures. There has been recent progress in developing syndrome-extraction circuits that tolerate qubit dropouts [76–79]; it would be interesting to see how these modified circuits affect the spin models—if lost qubits manifest as defects, and if so, what are their properties and effect on the phases of the SM models? Through our framework, these dynamical perspective can now all be readily understood through the perspective of statistical mechanics.

Our framework also opens conceptual directions for ex-

ploration. One of these concerns mixed-state phases of matter [16–19, 119–125], providing an alternative viewpoint on noise-resilient phases. This approach can also relate the decodability of a quantum code to classical SM systems, but instead of spins enumerating equivalent error strings consistent with a syndrome, they encode the syndrome itself when a codestate is subjected to an error channel. These mixed-state models are Kramers-Wannier duals to the SM models discussed in this paper, and the mapping from spacetime codes discussed here would follow analogously. The resulting models will describe a static mixed state in $(d+1)$ spatial dimensions—a counterpart of the time-evolving error-corrupted physical system in d spatial dimensions. (See also Ref. [52] for a mixed-state approach to fault tolerance via static $(d+1)$ D states.) It would be interesting to study how the corresponding information-theoretic quantities can capture features accounted for by our SM models.

From a broader perspective, our work contributes to the growing understanding that QEC is intimately connected to noise-resilient phases of matter. Static codes exhibit phase transitions between correctable and uncorrectable regimes; we have shown that this picture extends naturally to the full dynamical setting of circuits in spacetime. By investigating the spin models, we may reveal connections and dualities between initially-unrelated circuits and codes. As QEC moves from theoretical constructs to experimental implementations, tools that bridge circuit-level dynamics and statistical mechanics will prove increasingly valuable for understanding and optimizing fault-tolerant quantum computation.

ACKNOWLEDGMENTS

CA thanks Alaric Sanders for helpful discussions on Monte Carlo simulations. This research was supported by the Gates Cambridge Trust and by EPSRC grant EP/V062654/1.

- [1] A. Yu. Kitaev, Quantum Error Correction with Imperfect Gates, in *Quantum Communication, Computing, and Measurement*, edited by O. Hirota, A. S. Holevo, and C. M. Caves (Springer US, Boston, MA, 1997) pp. 181–188.
- [2] P. W. Shor, Fault-tolerant quantum computation (1997), [arXiv:quant-ph/9605011](https://arxiv.org/abs/quant-ph/9605011).
- [3] S. B. Bravyi and A. Y. Kitaev, Quantum codes on a lattice with boundary, [arXiv:quant-ph/9811052](https://arxiv.org/abs/quant-ph/9811052) (1998), [arXiv:quant-ph/9811052](https://arxiv.org/abs/quant-ph/9811052).
- [4] E. Knill, R. Laflamme, and W. H. Zurek, Resilient Quantum Computation, *Science* **279**, 342 (1998).
- [5] E. Dennis, A. Kitaev, A. Landahl, and J. Preskill, Topological quantum memory, *Journal of Mathematical Physics* **43**, 4452 (2002), [arXiv:quant-ph/0110143](https://arxiv.org/abs/quant-ph/0110143).
- [6] A. Y. Kitaev, Fault-tolerant quantum computation by anyons, *Annals of Physics* **303**, 2 (2003), [arXiv:quant-ph/9707021](https://arxiv.org/abs/quant-ph/9707021).
- [7] D. Aharonov and M. Ben-Or, Fault-Tolerant Quantum Computation with Constant Error Rate, *SIAM Journal on Computing* **38**, 1207 (2008).
- [8] D. E. Gottesman, *Stabilizer Codes and Quantum Error Correction*, Ph.D. thesis, California Institute of Technology (1997).
- [9] A. M. Steane, Error Correcting Codes in Quantum Theory, *Physical Review Letters* **77**, 793 (1996).
- [10] J. Preskill, Fault-Tolerant Quantum Computation, in *Introduction to Quantum Computation and Information* (WORLD SCIENTIFIC, 1998) pp. 213–269.
- [11] D. Poulin, Stabilizer Formalism for Operator Quantum Error Correction, *Physical Review Letters* **95**, 230504 (2005), [arXiv:quant-ph/0508131](https://arxiv.org/abs/quant-ph/0508131).

[12] H. Bombin, Topological subsystem codes, *Physical Review A* **81**, 032301 (2010).

[13] H. Bombin, R. S. Andrist, M. Ohzeki, H. G. Katzgraber, and M. A. Martin-Delgado, Strong Resilience of Topological Codes to Depolarization, *Physical Review X* **2**, 021004 (2012).

[14] A. Kubica, M. E. Beverland, F. Brandão, J. Preskill, and K. M. Svore, Three-Dimensional Color Code Thresholds via Statistical-Mechanical Mapping, *Physical Review Letters* **120**, 180501 (2018).

[15] C. T. Chubb and S. T. Flammia, Statistical mechanical models for quantum codes with correlated noise, *Annales de l'Institut Henri Poincaré D, Combinatorics, Physics and their Interactions* **8**, 269 (2021).

[16] Y. Bao, R. Fan, A. Vishwanath, and E. Altman, Mixed-state topological order and the errorfield double formulation of decoherence-induced transitions (2023), arXiv:2301.05687 [quant-ph].

[17] R. Fan, Y. Bao, E. Altman, and A. Vishwanath, Diagnostics of Mixed-State Topological Order and Breakdown of Quantum Memory, *PRX Quantum* **5**, 020343 (2024).

[18] S. Lee and E.-G. Moon, Mixed-State Topological Order under Coherent Noise, *PRX Quantum* **6**, 030355 (2025).

[19] S. Sang, Y. Zou, and T. H. Hsieh, Mixed-State Quantum Phases: Renormalization and Quantum Error Correction, *Physical Review X* **14**, 031044 (2024).

[20] F. Venn, J. Behrends, and B. Béria, Coherent-Error Threshold for Surface Codes from Majorana Delocalization, *Physical Review Letters* **131**, 060603 (2023).

[21] J. Behrends and B. Béria, Statistical Mechanical Mapping and Maximum-Likelihood Thresholds for the Surface Code under Generic Single-Qubit Coherent Errors, *PRX Quantum* **6**, 040305 (2025).

[22] J. Behrends and B. Béria, The Surface Code beyond Pauli Channels: Logical Noise Coherence, Information-Theoretic Measures, and Errorfield-Double Phenomenology, *PRX Quantum* **6**, 040350 (2025).

[23] Y. Bao and S. Anand, Phases of decodability in the surface code with unitary errors (2024), arXiv:2411.05785 [quant-ph].

[24] S. Sang and T. H. Hsieh, Stability of Mixed-State Quantum Phases via Finite Markov Length, *Physical Review Letters* **134**, 070403 (2025).

[25] L. Wichette, H. Hohenfeld, E. Mounzer, and L. Grans-Samuelsson, A partition function framework for estimating logical error curves in stabilizer codes (2025), arXiv:2505.15758 [quant-ph].

[26] L. H. English, S. Roberts, S. D. Bartlett, A. C. Doherty, and D. J. Williamson, Ising on the donut: Regimes of topological quantum error correction from statistical mechanics (2025), arXiv:2512.10399 [quant-ph].

[27] A. Lavasani and S. Vijay, Stability of gapped quantum matter and error-correction with adiabatic noise, *Physical Review Research* **7**, 023166 (2025).

[28] Z. Cheng, E. Huang, V. Khemani, M. J. Gullans, and M. Ippoliti, Emergent Unitary Designs for Encoded Qubits from Coherent Errors and Syndrome Measurements, *PRX Quantum* **6**, 030333 (2025).

[29] D. Jing, P. Sala, L. Jiang, and R. Verresen, Intrinsic Heralding and Optimal Decoders for Non-Abelian Topological Order (2025), arXiv:2507.23765 [quant-ph].

[30] E. Huang, P.-G. Rozon, A. Dua, S. Gopalakrishnan, and M. J. Gullans, A robust phase of continuous transversal gates in quantum stabilizer codes (2025), arXiv:2510.01319 [quant-ph].

[31] H. Liu and X. Chen, Coherent error induced phase transition (2025), arXiv:2506.00650 [quant-ph].

[32] J.-Z. Xu, Y. Zhong, M. A. Martin-Delgado, H. Song, and K. Liu, Phenomenological Noise Models and Optimal Thresholds of the 3D Toric Code (2025), arXiv:2510.20489 [quant-ph].

[33] Q. Wang, R. Vasseur, S. Trebst, A. W. W. Ludwig, and G.-Y. Zhu, Decoherence-induced self-dual criticality in topological states of matter (2025), arXiv:2502.14034 [quant-ph].

[34] E. H. Chen, G.-Y. Zhu, R. Verresen, A. Seif, E. Bäumer, D. Layden, N. Tantivasadakarn, G. Zhu, S. Sheldon, A. Vishwanath, S. Trebst, and A. Kandala, Nishimori transition across the error threshold for constant-depth quantum circuits, *Nature Physics* **21**, 161 (2025).

[35] J. Hauser, A. Lavasani, S. Vijay, and M. P. A. Fisher, Information dynamics and symmetry breaking in generic monitored \mathbb{Z}_2 -symmetric open quantum systems (2025), arXiv:2512.03031 [quant-ph].

[36] M. Pütz, R. Vasseur, A. W. W. Ludwig, S. Trebst, and G.-Y. Zhu, Flow to Nishimori universality in weakly monitored quantum circuits with qubit loss (2025), arXiv:2505.22720 [quant-ph].

[37] G.-Y. Zhu, N. Tantivasadakarn, A. Vishwanath, S. Trebst, and R. Verresen, Nishimori's Cat: Stable Long-Range Entanglement from Finite-Depth Unitaries and Weak Measurements, *Physical Review Letters* **131**, 200201 (2023).

[38] F. Eckstein, B. Han, S. Trebst, and G.-Y. Zhu, Learning transitions of topological surface codes (2025), arXiv:2512.19786 [quant-ph].

[39] M. B. Hastings and J. Haah, Dynamically Generated Logical Qubits, *Quantum* **5**, 564 (2021).

[40] J. Haah and M. B. Hastings, Boundaries for the Honeycomb Code, *Quantum* **6**, 693 (2022), arXiv:2110.09545 [quant-ph].

[41] Y. Tang and Y. Bao, Phases of Floquet code under local decoherence (2025), arXiv:2504.19041 [quant-ph].

[42] J. Claes, Dynamic circuit for the honeycomb Floquet code, *Physical Review A* **112**, 062406 (2025).

[43] D. Aasen, J. Haah, Z. Li, and R. S. K. Mong, Measurement Quantum Cellular Automata and Anomalies in Floquet Codes (2023), arXiv:2304.01277 [cond-mat, physics:math-ph, physics:quant-ph].

[44] T. D. Ellison, J. Sullivan, and A. Dua, Floquet codes with a twist (2023), arXiv:2306.08027 [quant-ph].

[45] M. Davydova, N. Tantivasadakarn, S. Balasubramanian, and D. Aasen, Quantum computation from dynamic automorphism codes, *Quantum* **8**, 1448 (2024).

[46] D. Vu, A. Lavasani, J. Y. Lee, and M. P. A. Fisher, Stable Measurement-Induced Floquet Enriched Topological Order, *Physical Review Letters* **132**, 070401 (2024), arXiv:2303.01533 [cond-mat, physics:quant-ph].

[47] C. T. Aitchison and B. Béria, Competing automorphisms and disordered Floquet codes, *Physical Review B* **111**, 235112 (2025).

[48] D. Vodola, M. Rispler, S. Kim, and M. Müller, Fundamental thresholds of realistic quantum error correction circuits from classical spin models, *Quantum* **6**, 618 (2022).

[49] Y. Xu, Y. Zhou, J. P. Sethna, and E.-A. Kim, Error thresholds of toric codes with transversal logical gates

(2025), arXiv:2510.10835 [quant-ph].

[50] M. H. Shaw and B. M. Terhal, Lowering Connectivity Requirements for Bivariate Bicycle Codes Using Morphing Circuits, *Physical Review Letters* **134**, 090602 (2025).

[51] G. M. Sommers, D. A. Huse, and M. J. Gullans, Dynamically generated concatenated codes and their phase diagrams, *Physical Review Research* **7**, 023086 (2025).

[52] A.-R. Negari, T. D. Ellison, and T. H. Hsieh, Spacetime Markov length: A diagnostic for fault tolerance via mixed-state phases (2024), arXiv:2412.00193 [quant-ph].

[53] F. Eckstein, B. Han, S. Trebst, and G.-Y. Zhu, Robust Teleportation of a Surface Code and Cascade of Topological Quantum Phase Transitions, *PRX Quantum* **5**, 040313 (2024).

[54] G.-Y. Zhu and S. Trebst, Qubit fractionalization and emergent Majorana liquid in the honeycomb Floquet code induced by coherent errors and weak measurements (2023), arXiv:2311.08450 [cond-mat, physics:quant-ph].

[55] M. Cain, D. Bluvstein, C. Zhao, S. Gu, N. Maskara, M. Kalinowski, A. A. Geim, A. Kubica, M. D. Lukin, and H. Zhou, Fast correlated decoding of transversal logical algorithms (2025), arXiv:2505.13587 [quant-ph].

[56] Á. Márton, L. Colmenarez, L. Bödeker, and M. Müller, Lattice surgery-based logical state teleportation via noisy links, *Physical Review Research* **7**, 033238 (2025).

[57] S. Chirame, A. Prem, S. Gopalakrishnan, and F. J. Burnell, Stabilizing Non-Abelian Topological Order Against Heralded Noise via Local Lindbladian Dynamics, *PRX Quantum* **6**, 030363 (2025).

[58] S. Chirame, F. J. Burnell, S. Gopalakrishnan, and A. Prem, Stable Symmetry-Protected Topological Phases in Systems with Heralded Noise, *Physical Review Letters* **134**, 010403 (2025).

[59] E. Takou and K. R. Brown, Estimating and decoding coherent errors of QEC experiments with detector error models (2025), arXiv:2510.23797 [quant-ph].

[60] G.-Y. Zhu, N. Tantivasadakarn, and S. Trebst, Structured volume-law entanglement in an interacting, monitored Majorana spin liquid, *Physical Review Research* **6**, L042063 (2024).

[61] D. Gottesman, Opportunities and Challenges in Fault-Tolerant Quantum Computation (2022), arXiv:2210.15844 [quant-ph].

[62] P.-J. H. S. Derks, A. Townsend-Teague, J. Eisert, M. S. Kesselring, O. Higgott, and B. J. Brown, Dynamical codes for hardware with noisy readouts (2025), arXiv:2505.07658 [quant-ph].

[63] M. Davydova, A. Bauer, J. C. M. de la Fuente, M. Webster, D. J. Williamson, and B. J. Brown, Universal fault tolerant quantum computation in 2D without getting tied in knots (2025), arXiv:2503.15751 [quant-ph].

[64] F. Setiawan and C. McLauchlan, Tailoring dynamical codes for biased noise: The X3Z3 Floquet code, *npj Quantum Information* **11**, 149 (2025).

[65] P.-J. H. S. Derks, A. Townsend-Teague, A. G. Burchards, and J. Eisert, Designing fault-tolerant circuits using detector error models (2024), arXiv:2407.13826 [quant-ph].

[66] D. J. Williamson and B. Hetényi, Dynamical quantum codes and logic gates on a lattice with sparse connectivity (2025), arXiv:2510.05225 [quant-ph].

[67] Y. Xu and A. Dua, Fault-tolerant protocols through spacetime concatenation (2025), arXiv:2504.08918 [quant-ph].

[68] A. Tanggara, M. Gu, and K. Bharti, Strategic Code: A Unified Spatio-Temporal Framework for Quantum Error-Correction (2024), arXiv:2405.17567 [quant-ph].

[69] A. Tanggara, M. Gu, and K. Bharti, Simple Construction of Qudit Floquet Codes on a Family of Lattices (2024), arXiv:2410.02022 [quant-ph].

[70] E. X. Fu and D. Gottesman, Error Correction in Dynamical Codes, *Quantum* **9**, 1886 (2025).

[71] G. Kishony and E. Berg, Increasing the distance of topological codes with time vortex defects (2025), arXiv:2502.12236 [quant-ph].

[72] H. Bombin, D. Litinski, N. Nickerson, F. Pastawski, and S. Roberts, Unifying flavors of fault tolerance with the ZX calculus, *Quantum* **8**, 1379 (2024).

[73] G. P. Gehér, C. McLauchlan, E. T. Campbell, A. E. Moylett, and O. Crawford, Error-corrected Hadamard gate simulated at the circuit level, *Quantum* **8**, 1394 (2024).

[74] M. McEwen, D. Bacon, and C. Gidney, Relaxing Hardware Requirements for Surface Code Circuits using Time-dynamics, *Quantum* **7**, 1172 (2023).

[75] A. Eickbusch, M. McEwen, V. Sivak, A. Bourassa, J. Atalaya, J. Claes, D. Kafri, C. Gidney, C. W. Warren, J. Gross, A. Opremcak, N. Zobrist, K. C. Miao, G. Roberts, K. J. Satzinger, A. Bengtsson, M. Neeley, W. P. Livingston, A. Greene, R. Acharya, L. Aghababaie Beni, G. Aigeldinger, R. Alcaraz, T. I. Andersen, M. Ansmann, F. Arute, K. Arya, A. Asfaw, R. Babbush, B. Ballard, J. C. Bardin, A. Bilmes, J. Bovaird, D. Bowers, L. Brill, M. Broughton, D. A. Browne, B. Buchea, B. B. Buckley, T. Burger, B. Burkett, N. Bushnell, A. Cabrera, J. Campero, H.-S. Chang, B. Chiaro, L.-Y. Chih, A. Y. Cleland, J. Coogan, R. Collins, P. Conner, W. Courtney, A. L. Crook, B. Curtin, S. Das, A. Del Toro Barba, S. Demura, L. De Lorenzo, A. Di Paolo, P. Donohoe, I. K. Drozdov, A. Dunsworth, A. M. Elbag, M. Elzouka, C. Erickson, V. S. Ferreira, L. Flores Burgos, E. Forati, A. G. Fowler, B. Foxen, S. Ganjam, G. Garcia, R. Gasca, É. Genois, W. Giang, D. Gilboa, R. Gosula, A. Grajales Dau, D. Graumann, T. Ha, S. Habegger, M. C. Hamilton, M. Hansen, M. P. Harrigan, S. D. Harrington, S. Heslin, P. Heu, O. Higgott, R. Hiltermann, J. Hilton, H.-Y. Huang, A. Huff, W. J. Huggins, E. Jeffrey, Z. Jiang, X. Jin, C. Jones, C. Joshi, P. Juhas, A. Kabel, H. Kang, A. H. Karamlou, K. Kechedzhi, T. Khaire, T. Khatkar, M. Khezri, S. Kim, B. Kobrin, A. N. Korotkov, F. Kostritsa, J. M. Kreikebaum, V. D. Kurilovich, D. Landhuis, T. Lange-Dei, B. W. Langley, K.-M. Lau, J. Ledford, K. Lee, B. J. Lester, L. Le Guevel, W. Y. Li, A. T. Lill, A. Locharla, E. Lucero, D. Lundahl, A. Lunt, S. Madhuk, A. Maloney, S. Mandrà, L. S. Martin, O. Martin, C. Maxfield, J. R. McClean, S. Meeks, A. Megrant, R. Molavi, S. Molina, S. Montaz-eri, R. Movassagh, M. Newman, A. Nguyen, M. Nguyen, C.-H. Ni, L. Oas, R. Orosco, K. Ottosson, A. Pizzuto, R. Potter, O. Pritchard, C. Quintana, G. Ramachandran, M. J. Reagor, D. M. Rhodes, E. Rosenberg, E. Rossi, K. Sankaragomathi, H. F. Schurkus, M. J. Shearn, A. Shorter, N. Shutty, V. Shvarts, S. Small, W. C. Smith, S. Springer, G. Sterling, J. Suchard,

A. Szasz, A. Sztein, D. Thor, E. Tomita, A. Torres, M. M. Torunbalci, A. Vaishnav, J. Vargas, S. Vdovichev, G. Vidal, C. Vollgraff Heidweiller, S. Waltman, J. Waltz, S. X. Wang, B. Ware, T. Weidel, T. White, K. Wong, B. W. K. Woo, M. Woodson, C. Xing, Z. J. Yao, P. Yeh, B. Ying, J. Yoo, N. Yosri, G. Young, A. Zalcman, Y. Zhang, N. Zhu, S. Boixo, J. Kelly, V. Smelyanskiy, H. Neven, D. Bacon, Z. Chen, P. V. Klimov, P. Roushan, C. Neill, Y. Chen, and A. Morvan, Demonstration of dynamic surface codes, *Nature Physics* **21**, 1994 (2025).

[76] D. M. Debroy, M. McEwen, C. Gidney, N. Shutty, and A. Zalcman, LUCI in the Surface Code with Dropouts (2024), arXiv:2410.14891 [quant-ph].

[77] A. Strikis, S. C. Benjamin, and B. J. Brown, Quantum Computing is Scalable on a Planar Array of Qubits with Fabrication Defects, *Physical Review Applied* **19**, 064081 (2023).

[78] B. Anker and D. M. Debroy, Optimized Measurement Schedules for the Surface Code with Dropout (2025), arXiv:2512.10871 [quant-ph].

[79] S. Wolanski, Automated Compilation Including Dropouts: Tolerating Defective Components in Stabiliser Codes (2025), arXiv:2512.01943 [quant-ph].

[80] S. Martiel and A. Javadi-Abhari, Low-overhead error detection with spacetime codes (2025), arXiv:2504.15725 [quant-ph].

[81] C. Gidney and D. Bacon, Less Bacon More Threshold (2023), arXiv:2305.12046 [quant-ph].

[82] K. Sahay, Y. Lin, S. Huang, K. R. Brown, and S. Puri, Error Correction of Transversal cnot Gates for Scalable Surface-Code Computation, *PRX Quantum* **6**, 020326 (2025).

[83] M. Serra-Peralta, M. H. Shaw, and B. M. Terhal, Decoding across transversal Clifford gates in the surface code (2025), arXiv:2505.13599 [quant-ph].

[84] M. E. Beverland, S. Huang, and V. Kliuchnikov, Fault tolerance of stabilizer channels (2024), arXiv:2401.12017 [quant-ph].

[85] N. Delfosse and A. Paetznick, Spacetime codes of Clifford circuits (2023), arXiv:2304.05943 [quant-ph].

[86] D. Bacon, S. T. Flammia, A. W. Harrow, and J. Shi, Sparse Quantum Codes from Quantum Circuits, in *IEEE Transactions on Information Theory*, 4, Vol. 63 (2017) pp. 2464–2479, arXiv:1411.3334 [quant-ph].

[87] A. Pesah, A. K. Daniel, I. Tzitrin, and M. Vassmer, Fault-tolerant transformations of spacetime codes (2025), arXiv:2509.09603 [quant-ph].

[88] X. Fu and D. Gottesman, Subsystem Spacetime Code (2025).

[89] J. C. Bridgeman and C. T. Chubb, Hand-waving and Interpretive Dance: An Introductory Course on Tensor Networks, *Journal of Physics A: Mathematical and Theoretical* **50**, 223001 (2017), arXiv:1603.03039 [cond-mat, physics:hep-th, physics:quant-ph].

[90] J. van de Wetering, ZX-calculus for the working quantum computer scientist (2020), arXiv:2012.13966 [quant-ph].

[91] M. Rüsch, B. Rodatz, and A. Kissinger, Completeness for Fault Equivalence of Clifford ZX Diagrams (2025), arXiv:2510.08477 [quant-ph].

[92] C. Gidney, M. Newman, and M. McEwen, Benchmarking the Planar Honeycomb Code, *Quantum* **6**, 813 (2022).

[93] L. H. English, D. J. Williamson, and S. D. Bartlett, Thresholds for post-selected quantum error correction from statistical mechanics (2024), arXiv:2410.07598 [quant-ph].

[94] S. Bravyi, M. Suchara, and A. Vargo, Efficient Algorithms for Maximum Likelihood Decoding in the Surface Code, *Physical Review A* **90**, 032326 (2014), arXiv:1405.4883 [quant-ph].

[95] C. Gidney, Stability Experiments: The Overlooked Dual of Memory Experiments, *Quantum* **6**, 786 (2022).

[96] C. Gidney, Stim: A fast stabilizer circuit simulator, *Quantum* **5**, 497 (2021).

[97] O. Higgott and C. Gidney, Sparse Blossom: Correcting a million errors per core second with minimum-weight matching, *Quantum* **9**, 1600 (2025).

[98] Y. Li, N. O’Dea, and V. Khemani, Perturbative Stability and Error-Correction Thresholds of Quantum Codes, *PRX Quantum* **6**, 010327 (2025).

[99] L. Grans-Samuelsson, R. V. Mishmash, D. Aasen, C. Knapp, B. Bauer, B. Lackey, M. P. D. Silva, and P. Bonderson, Improved Pairwise Measurement-Based Surface Code, *Quantum* **8**, 1429 (2024).

[100] L. Grans-Samuelsson, D. Aasen, and P. Bonderson, Fault-tolerant pairwise measurement-based code on eight qubits, *Physical Review A* **112**, 042413 (2025).

[101] A. Honecker, M. Picco, and P. Pujol, Universality Class of the Nishimori Point in the $2D \pm J$ Random-Bond Ising Model, *Physical Review Letters* **87**, 047201 (2001).

[102] F. Merz and J. T. Chalker, Two-dimensional random-bond Ising model, free fermions, and the network model, *Physical Review B* **65**, 054425 (2002).

[103] N. Kawashima and T. Aoki, Zero-Temperature Critical Phenomena in Two-Dimensional Spin Glasses (1999), arXiv:cond-mat/9911120.

[104] C. Wang, J. Harrington, and J. Preskill, Confinement-Higgs transition in a disordered gauge theory and the accuracy threshold for quantum memory, *Annals of Physics* **303**, 31 (2003).

[105] A. G. Fowler, A. M. Stephens, and P. Groszkowski, High-threshold universal quantum computation on the surface code, *Physical Review A* **80**, 052312 (2009).

[106] M. Ohzeki, Error threshold estimates for surface code with loss of qubits, *Physical Review A* **85**, 060301 (2012).

[107] K. Blackwell and J. Haah, The code distance of Floquet codes (2025), arXiv:2510.05549 [quant-ph].

[108] M. S. Alam and E. Rieffel, Dynamical Logical Qubits in the Bacon-Shor Code (2024), arXiv:2403.03291 [quant-ph].

[109] M. S. Kesselring, J. C. Magdalena De La Fuente, F. Thomsen, J. Eisert, S. D. Bartlett, and B. J. Brown, Anyon Condensation and the Color Code, *PRX Quantum* **5**, 010342 (2024), arXiv:2212.00042 [cond-mat, physics:quant-ph].

[110] B. Rodatz, B. Poór, and A. Kissinger, Floquetifying stabiliser codes with distance-preserving rewrites (2024), arXiv:2410.17240 [quant-ph].

[111] E. Sutcliffe, B. Jonnadula, C. L. Gall, A. E. Moylett, and C. M. Westoby, Distributed quantum error correction based on hyperbolic Floquet codes (2025), arXiv:2501.14029 [quant-ph].

[112] Z. Zhang, D. Aasen, and S. Vijay, X-cube Floquet code: A dynamical quantum error correcting code with a subextensive number of logical qubits, *Physical Review B* **108**, 205116 (2023).

[113] D. Aasen, J. Haah, P. Bonderson, Z. Wang, and M. Hastings, Fault-Tolerant Hastings-Haah Codes in the Presence of Dead Qubits (2023), [arXiv:2307.03715 \[quant-ph\]](https://arxiv.org/abs/2307.03715).

[114] A. Dua, N. Tantivasadakarn, J. Sullivan, and T. D. Ellison, Engineering 3D Floquet Codes by Rewinding, *PRX Quantum* **5**, 020305 (2024).

[115] C. McLauchlan, G. P. Gehér, and A. E. Moylett, Accommodating Fabrication Defects on Floquet Codes with Minimal Hardware Requirements (2024), [arXiv:2405.15854 \[quant-ph\]](https://arxiv.org/abs/2405.15854).

[116] M. Davydova, N. Tantivasadakarn, and S. Balasubramanian, Floquet Codes without Parent Subsystem Codes, *PRX Quantum* **4**, 020341 (2023).

[117] V. Motamarri, C. McLauchlan, and B. Béri, SymTFT out of equilibrium: From time crystals to braided drives and Floquet codes (2024), [arXiv:2312.17176 \[cond-mat, physics:hep-th, physics:quant-ph\]](https://arxiv.org/abs/2312.17176).

[118] A. E. Moylett and B. Jonnadula, Logical gates on Floquet codes via folds and twists (2025), [arXiv:2512.17999 \[quant-ph\]](https://arxiv.org/abs/2512.17999).

[119] A. Lyons, Understanding Stabilizer Codes Under Local Decoherence Through a General Statistical Mechanics Mapping (2024), [arXiv:2403.03955 \[quant-ph\]](https://arxiv.org/abs/2403.03955).

[120] Z. Li and R. S. K. Mong, Replica topological order in quantum mixed states and quantum error correction (2024), [arXiv:2408.05001 \[quant-ph\]](https://arxiv.org/abs/2408.05001).

[121] R. Sohal and A. Prem, Noisy Approach to Intrinsically Mixed-State Topological Order, *PRX Quantum* **6**, 010313 (2025).

[122] T. Rakovszky, S. Gopalakrishnan, and C. Von Keyserlingk, Defining Stable Phases of Open Quantum Systems, *Physical Review X* **14**, 041031 (2024).

[123] R. Luo, Y.-N. Wang, and Z. Bi, Topological Holography for Mixed-State Phases and Phase Transitions, *PRX Quantum* **6**, 040358 (2025).

[124] Y.-H. Chen and T. Grover, Separability Transitions in Topological States Induced by Local Decoherence, *Physical Review Letters* **132**, 170602 (2024).

[125] L. A. Lessa, R. Ma, J.-H. Zhang, Z. Bi, M. Cheng, and C. Wang, Strong-to-Weak Spontaneous Symmetry Breaking in Mixed Quantum States, *PRX Quantum* **6**, 010344 (2025).

[126] N. G. Berloff, Exact Spin Elimination in Ising Hamiltonians and Energy-Based Machine Learning (2025), [arXiv:2505.07163 \[quant-ph\]](https://arxiv.org/abs/2505.07163).

[127] C. H. Bennett, Efficient estimation of free energy differences from Monte Carlo data, *Journal of Computational Physics* **22**, 245 (1976).

[128] A. F. Voter, A Monte Carlo method for determining free-energy differences and transition state theory rate constants, *The Journal of Chemical Physics* **82**, 1890 (1985).

Appendix A: Additional details

1. Spacetime codes

In this section, we continue our discussion of spacetime codes.

a. Stabilizers and logical operators To define the spacetime stabilizers and logical operators, we first define the propagator superoperator $\Pi_{\tau \rightarrow \tau'}$ that takes a $[Q]_{,\tau} \in \mathcal{P}_{\text{st}}$ and multiplies it by gauge operators until it has support only at half-integer time τ' (if possible¹³). That is, $\Pi_{\tau \rightarrow \tau'}[Q] \equiv [Q']_{,\tau'}$ for some new $Q' \in \mathcal{P}_{\text{ph}}$.

Related to the propagator is the cumulant superoperator, $\overrightarrow{\cdot}$, which creates a spacetime operator whose action on the qubits at a half-integer time is the cumulative effect of propagating forward all operators prior to that time.¹⁴ Specifically, the cumulant of a spacetime operator that has nontrivial support on only one half-integer timestep is defined as

$$\overrightarrow{[Q]_{,\tau}} = \prod_{\tau'=\tau}^{T-0.5} \Pi_{\tau \rightarrow \tau'}[Q] \in \mathcal{P}_{\text{st}}. \quad (\text{A1})$$

The cumulant is an automorphism of \mathcal{P}_{st} [85]; for $F, G \in \mathcal{P}_{\text{st}}$, it obeys $\overrightarrow{FG} = \overrightarrow{F}\overrightarrow{G}$. For a general $F \in \mathcal{P}_{\text{st}}$ that acts as $F_\tau \in \mathcal{P}_{\text{ph}}$ at each half-integer time τ —that is, $F = \prod_{\tau=0.5}^{T-0.5} [F_\tau]_{,\tau}$ —we thus have

$$\overrightarrow{F} = \prod_{\tau=0.5}^{T-0.5} \overrightarrow{[F_\tau]_{,\tau}}. \quad (\text{A2})$$

The cumulant defines the stabilizers and logical operators of the spacetime code, as we shall describe now.

For a Pauli measurement $M_\xi \in \mathcal{P}_{\text{ph}}$ that occurs at t_ξ in the circuit, let $o(M_\xi)$ be its measurement outcome when the circuit is executed in the absence of errors. Depending on the circuit, this outcome may either be a deterministic

¹³ In the absence of mid-circuit measurements, this is always possible by applying Eq. (9).

¹⁴ Also known as the “spackle” superoperator.

value—that is, M_ξ always gives the same outcome because the system is in its eigenstate when measured—or non-deterministic. If individual outcomes are non-deterministic, their product may still be deterministic if the product of the associated M_ξ is an eigenoperator. For a set of measurement indices $\Xi_k = \{\xi\}$, if the product $\mathcal{O}_k = \prod_{\xi \in \Xi_k} o(M_\xi)$ is deterministic, observing a different outcome indicates that an error occurred in the support of $\{M_\xi\}$. We use this property to define the stabilizers of the spacetime code,

$$S_k = \overrightarrow{M}_{(k)} \mathcal{O}_k, \quad (\text{A3})$$

where

$$M_{(k)} = \prod_{\xi \in \Xi_k} [M_\xi]_{,t_\xi+0.5}. \quad (\text{A4})$$

The multiplication by \mathcal{O}_k ensures that the eigenvalue of S_k is $+1$ in the absence of errors, and the cumulant ensures that S_k anticommutes with all errors that would change the outcome of the measurements in $M_{(k)}$.

In a circuit that measures the syndromes of a QEC code, these $M_{(k)}$ take the form of two consecutive measurements of a stabilizer. These are equivalent to detector cells [61, 65, 74], which are generalizations of stabilizers to circuits: pairs of stabilizer measurements that signal an error whenever an outcome changes. The logical operators of the spacetime code are then the cumulants of the logical operators of the QEC code. Specifically, if a logical operator is $L(t)$ at timestep t of a circuit (where the operator may evolve according to an automorphism in a Floquet code, for example), then the spacetime logical operator is the membrane

$$\overrightarrow{L} = \prod_{t=0}^T [L(t)]_{,t+0.5}. \quad (\text{A5})$$

If we have two logical operators L_1, L_2 such that $\llbracket L_1(t), L_2(t) \rrbracket = -1$ for all t , then $\llbracket \overrightarrow{L}_1, \overrightarrow{L}_2 \rrbracket = -1$ iff T is even [86].¹⁵ If T is odd, we may simply double it to achieve correct anticommutation. Since we are typically concerned with the $T \rightarrow \infty$ bulk behavior, we assume without loss of generality that T is even.

These logical membranes are the bare logical operators of the spacetime subsystem code, in that they commute with all stabilizers and the gauge group, but are not in the gauge group. The dressed logical operators, however, typically take a simpler structure. In particular, $[L(t_1)]_{,t_1+0.5}$ and $[L(t_2)]_{,t_2+0.5}$ are gauge-equivalent, as the gauge operators encode propagations in spacetime. If T is even, we thus have that \overrightarrow{L} is gauge-equivalent to $[L(t)]_{,t+0.5}$ for any $t \in [0, T]$. That is, the dressed spacetime logical operators include the original code's logical operators on a single timeslice.

b. Subsystem codes When the Clifford circuit describes the syndrome measurement circuit of a stabilizer code, the two types of gauge generators discussed in the main text do indeed generate the spacetime gauge group. However, in a syndrome circuit of a subsystem code there are additional gauge freedoms not captured. Specifically, the gauge generators of the static subsystem code at each timestep need to be determined by considering the stabilizers measured by the circuit; these will add spacelike spacetime gauge operators [88]. One can check if all such operators have been added—or if they are necessary in the first place given an unknown Clifford circuit—by, for example, using Stim to search for low-weight undetectable errors [96].

2. SM mapping

The error-string model ultimately aims to relate the partition function of some quenched-disordered classical random-bond model to the probability of a class of logical errors. Specifically, define the logical coset

$$\overline{E} = E\mathcal{G} \quad (\text{A6})$$

for some Pauli error E , and \mathcal{G} the gauge group (the following analysis proceeds identically if we replace \mathcal{G} by the stabilizer group). We wish to compute the probability

$$\mathbb{P}(\overline{E}) = \sum_{\epsilon \in E\mathcal{G}} \mathbb{P}(\epsilon). \quad (\text{A7})$$

¹⁵ If T is odd, then the logical operator in Eq. (A5) is in the gauge group and the code is trivial.

If $\epsilon_i \in \mathcal{P}_i = \{I, X, Y, Z\}$ is a single-qubit Pauli error on qubit i , then we can write its probability in the form

$$\begin{aligned} \mathbb{P}(\epsilon_i) &= \left[\left(\frac{\mathbb{P}(I)\mathbb{P}(X)}{\mathbb{P}(Y)\mathbb{P}(Z)} \right)^{[\epsilon_i, X]} \left(\frac{\mathbb{P}(I)\mathbb{P}(Y)}{\mathbb{P}(X)\mathbb{P}(Z)} \right)^{[\epsilon_i, Y]} \left(\frac{\mathbb{P}(I)\mathbb{P}(Z)}{\mathbb{P}(X)\mathbb{P}(Y)} \right)^{[\epsilon_i, Z]} \mathbb{P}(I)\mathbb{P}(X)\mathbb{P}(Y)\mathbb{P}(Z) \right]^{1/4} \\ &= \exp \left[\frac{1}{4} \sum_{\alpha \in \mathcal{P}_i} \sum_{\tau \in \mathcal{P}_i} \ln [\mathbb{P}(\tau)] [\alpha, \tau] [\epsilon_i, \alpha] \right] \\ &\equiv \exp \left[\sum_{\alpha \in \mathcal{P}_i} K_i(\alpha) [\epsilon_i, \alpha] \right]; \quad K_i(\alpha) = \frac{1}{4} \sum_{\tau \in \mathcal{P}_i} \ln [\mathbb{P}(\tau)] [\alpha, \tau]. \end{aligned} \quad (\text{A8})$$

For the total error string $\epsilon = \otimes_i \epsilon_i$, we therefore have

$$\mathbb{P}(\epsilon) = \prod_i \mathbb{P}(\epsilon_i) = \exp \left[\sum_i \sum_{\alpha \in \mathcal{P}_i} K_i(\alpha) [\epsilon, \alpha] \right] \equiv e^{-H_0}, \quad (\text{A9})$$

where

$$H_0 = - \sum_i \sum_{\alpha \in \mathcal{P}_i} K_i(\alpha) [\epsilon, \alpha]. \quad (\text{A10})$$

Now, any errors $\epsilon, \epsilon' \in E\mathcal{G}$ are related by a product of gauge operators, $\epsilon' = g\epsilon$, $g \in \mathcal{G}$. If $\mathcal{G} = \langle g_1, g_2, \dots, g_\gamma \rangle$ is generated by γ gauge operators g_k then we can represent $E\mathcal{G}$ by γ -bit binary vectors $\mathbf{b} \in \mathbb{B}_\gamma = \{0, 1\}^\gamma$, as

$$\epsilon_{\mathbf{b}} = E \prod_{k=1}^{\gamma} g_k^{\mathbf{b}_k}. \quad (\text{A11})$$

For some Pauli $\alpha \in \mathcal{P}$, the scalar commutator acts on this representation as

$$\begin{aligned} [\epsilon_{\mathbf{b}}, \alpha] &= [E, \alpha] \prod_{k=1}^{\gamma} [g_k, \alpha]^{\mathbf{b}_k} \\ &= [E, \alpha] \prod_{k: [g_k, \alpha] = -1} (-1)^{\mathbf{b}_k}. \end{aligned} \quad (\text{A12})$$

Therefore,

$$\mathbb{P}(\overline{E}) = \sum_{\mathbf{b} \in \mathbb{B}_\gamma} e^{-H_E(\mathbf{b})}, \quad (\text{A13})$$

where

$$H_E(\mathbf{b}) = - \sum_i \sum_{\alpha \in \mathcal{P}_i} K_i(\alpha) [E, \alpha] \prod_{k: [g_k, \alpha] = -1} (-1)^{\mathbf{b}_k}. \quad (\text{A14})$$

Identifying classical Ising spins $\sigma_k = (-1)^{\mathbf{b}_k}$ thus brings us to the Hamiltonian in Eq. (14).

a. Discrete Walsh transform

In this section we detail how spins can be integrated out of the Hamiltonian in order to simplify the model. We wish to integrate out spin σ_0 from a Hamiltonian of the form

$$H = H_0 - \sigma_0 P(\Sigma) \quad (\text{A15})$$

where H_0 is independent of σ_0 , and P encodes the σ_0 -dependent interactions

$$P(\Sigma) = \sum_{i=1}^r K_i \Sigma_i \quad (\text{A16})$$

where $\Sigma = [\Sigma_1, \dots, \Sigma_r] \in \{-1, 1\}^r$ is a product of spins and interactions signs. For example, if $r = 1$ (spin σ_0 is involved in only one interaction, i.e. it is degree-1),

$$\Sigma = [\eta_1 \sigma_1], \quad P(\Sigma) = K_1 \eta_1 \sigma_1, \quad (\text{A17})$$

or if $r = 2$,

$$\Sigma = [\eta_1 \sigma_1, \eta_2 \sigma_2], \quad P(\Sigma) = K_1 \eta_1 \sigma_1 + K_2 \eta_2 \sigma_2. \quad (\text{A18})$$

Tracing out σ_0 , we get an effective Hamiltonian

$$\begin{aligned} \sum_{\sigma_0 \in \{-1, 1\}} e^{-H} &= e^{-H_0} \left(e^{P(\Sigma)} + e^{-P(\Sigma)} \right) \\ &= 2e^{-H_0} \cosh [P(\Sigma)] \\ &= e^{-H_0 + \ln \cosh [P(\Sigma)] + \ln 2} \\ H_{\text{eff}} &= H_0 - f(\Sigma) \end{aligned} \quad (\text{A19})$$

where

$$f(\Sigma) = \ln \cosh [P(\Sigma)], \quad (\text{A20})$$

and we ignore the constant contribution. When $r = 1$, $\cosh(P(\Sigma)) = \cosh |K_1 \eta_1 \sigma_1|$ is independent of $\eta_1 \sigma = \pm 1$ and we are left with $H_{\text{eff}} = H_0$ up to constants. In this way, degree-1 spins and their sole interaction term can be removed from the Hamiltonian without affecting the partition function (up to an unimportant pre-factor).

For $r > 1$, we cannot remove $f(\Sigma)$ and we instead aim to write $f(\Sigma)$ as a linear combination of Σ_i . To do so, we define Walsh coefficients

$$F(S) = \frac{1}{2^r} \sum_{\theta \in \{-1, 1\}^r} f(\theta) \prod_{i \in S} \theta_i, \quad S \subseteq \{1, 2, \dots, r\} \quad (\text{A21})$$

where S is an index set that determines which components θ_i of θ are included. A summation over all non-empty S recovers $f(\Sigma)$ (up to constant terms) [126]

$$H_{\text{eff}} = H_0 - \sum_{S \neq \emptyset} F(S) \prod_{i \in S} \Sigma_i. \quad (\text{A22})$$

For example, taking $r = 2$ and using P from Eq. (A18), we get

$$f(\{-1, -1\}) = f(\{1, 1\}) = \ln \cosh(K_1 + K_2), \quad (\text{A23})$$

$$f(\{-1, 1\}) = f(\{1, -1\}) = \ln \cosh |K_1 - K_2| \quad (\text{A24})$$

$$F(\{1\}) = F(\{2\}) = 0 \quad (\text{A25})$$

$$F(\{1, 2\}) = \frac{1}{2} \ln \cosh(K_1 + K_2) - \frac{1}{2} \ln \cosh |K_1 - K_2|, \quad (\text{A26})$$

which results in an effective Hamiltonian

$$H_{\text{eff}} = H_0 - \frac{1}{2} \ln \left(\frac{\cosh(K_1 + K_2)}{\cosh |K_1 - K_2|} \right) \eta_1 \eta_2 \sigma_1 \sigma_2. \quad (\text{A27})$$

Now, assume that

$$K_i = \frac{1}{2} \ln \left(\frac{1 - p_i}{p_i} \right) \equiv \frac{1}{2} \ln \left(\frac{1 + \pi_i}{1 - \pi_i} \right), \quad (\text{A28})$$

for some $\pi_i \in (0, 1)$ and $p_i = \frac{1}{2}(1 - \pi_i)$. Then,

$$\frac{\cosh(K_1 + K_2)}{\cosh|K_1 - K_2|} = \frac{e^{K_1}e^{K_2} + e^{-K_1}e^{-K_2}}{e^{K_1}e^{-K_2} + e^{-K_1}e^{K_2}} \quad (\text{A29})$$

$$= \frac{\sqrt{\frac{1+\pi_1}{1-\pi_1} \frac{1+\pi_2}{1-\pi_2}} + \sqrt{\frac{1-\pi_1}{1+\pi_1} \frac{1-\pi_2}{1+\pi_2}}}{\sqrt{\frac{1+\pi_1}{1-\pi_1} \frac{1-\pi_2}{1+\pi_2}} + \sqrt{\frac{1-\pi_1}{1+\pi_1} \frac{1+\pi_2}{1-\pi_2}}} \quad (\text{A30})$$

$$= \frac{(1 + \pi_1)(1 + \pi_2) + (1 - \pi_1)(1 - \pi_2)}{(1 + \pi_1)(1 - \pi_2) + (1 - \pi_1)(1 + \pi_2)} \quad (\text{A31})$$

$$= \frac{1 + \pi_1\pi_2}{1 - \pi_1\pi_2} \quad (\text{A32})$$

$$\equiv \frac{1 - p_{1,2}}{p_{1,2}}, \quad p_{1,2} = \frac{1}{2}(1 - \pi_1\pi_2). \quad (\text{A33})$$

If $\pi_i = (1 - 2p_X)^{x_i}(1 - 2p_Z)^{z_i}$ for some non-negative integers x_i, z_i , then this recovers the effective probability parameters from Eq. (24). Substituting this back into the effective Hamiltonian brings us to the form of the effective interaction strength from Eq. (25).

When $r \geq 3$, the number of nonzero $F(S)$, and therefore the number of interactions in the effective Hamiltonian, is generally larger than r . We thus do not consider integrating out spins involved in more than two interactions; this also limits this procedure to independent X - Z noise channels. Otherwise, contribution from $J(Y)$ terms increase the number of interactions each spin undergoes, and restrict this procedure to single-qubit gauge operators.

Appendix B: Numerical methods

1. Monte Carlo

Monte Carlo simulations are used to estimate the success (or failure) probabilities of a maximum likelihood decoder for each quantum circuit. This amounts to computing the free-energy differences between systems with quenched disorders corresponding to distinct logical classes. By Eq. (8) and Eq. (15), the success probability of an ML decoder is given by

$$\mathbb{P}(\text{success}) = \left\langle \frac{\max_L\{e^{-F_{C_sL}}\}}{\sum_L e^{-F_{C_sL}}} \right\rangle_{\eta} \equiv \left\langle \frac{\max_L\{e^{-(F_{C_sL} - F_{C_s})}\}}{\sum_L e^{-(F_{C_sL} - F_{C_s})}} \right\rangle_{\eta} \quad (\text{B1})$$

where $\langle \cdot \rangle_{\eta}$ is the average over quenched disorders according to the probability distribution of η . The latter formula is used when computing free-energy differences is preferable. Each free energy is computable from

$$F_E = -\ln \mathcal{Z}_E = -\ln \langle e^{-H_E} \rangle_{\beta} \quad (\text{B2})$$

where \mathcal{Z}_E is the partition function and $\langle \cdot \rangle_{\beta}$ is the thermal average at a given quenched disorder.

We employ two approaches to estimate these free energies.

a. Parallel tempering. Parallel tempering (or replica exchange Monte Carlo) improves upon the standard Metropolis-Hastings algorithm with reduced critical slowing down near phase transitions. For a given disorder realization, we maintain R replicas (typically $10 - 100$) of the system at inverse temperatures $\beta_1 = 1, \dots, \beta_R$. All replicas share the same quenched bond disorder but evolve independently via single-spin Metropolis updates. After each sweep of the system (order N updates, where N is the total number of spins), we attempt replica exchanges between replicas of adjacent temperatures $i, i + 1$ using the Metropolis criterion

$$\mathbb{P}(\text{accept}) = \min \left\{ 1, e^{(\beta_{i+1} - \beta_i)(\mathcal{E}_{i+1} - \mathcal{E}_i)} \right\} \quad (\text{B3})$$

where \mathcal{E}_i is the energy of replica i . This maintains detailed balance of the simulation while enabling configurations to diffuse through temperature space. Colder replicas borrow entropy from hotter replicas and more readily escape local energy minima.

The free-energy F_{C_sL} is slow to compute due to the exponential function being dominated by high-energy but improbable configurations. We instead use the multi-step Bennett acceptance ratio [127, 128]: to estimate $F_{C_sL} - F_{C_s}$,

we decompose L into M “components”

$$L_\mu = \prod_{m=1}^{\mu} Q_m, \quad L_0 = I, \quad L_M = L \quad (\text{B4})$$

where each $Q_m \in \mathcal{P}_{\text{st}}$ is a (small) Pauli operator (e.g., a single-qubit Pauli). Then, we reduce the free-energy estimation to a product of smaller ratios

$$F_{C_s L} - F_{C_s} = -\ln \frac{\mathcal{Z}_{C_s L}}{\mathcal{Z}_{C_s}} = -\ln \left[\prod_{m=1}^M \frac{\mathcal{Z}_{C_s L_m}}{\mathcal{Z}_{C_s L_{m-1}}} \right]. \quad (\text{B5})$$

We simulate $(M+1)$ β -ladders of R replicas each with quenched disorder given by $C_s, C_s L_1, \dots, C_s L$ and compute

$$\frac{\mathcal{Z}_{C_s L_m}}{\mathcal{Z}_{C_s L_{m-1}}} = \frac{\langle f(C_s L_m; C_s L_{m-1}) \rangle_\beta}{\langle f(C_s L_{m-1}; C_s L_m) \rangle_\beta}, \quad f(E; E') = \min \left\{ 1, e^{-\Delta\mathcal{E}(E; E')} \right\} \quad (\text{B6})$$

where $\Delta\mathcal{E}(E; E')$ is the energy difference acquired by placing the spins from the replica evolving under quenched disorder E' (at temperature β_1) onto the Hamiltonian with quenched disorder E (unlike replica exchange, this swap does not follow through; we record only the energy difference if the swap were to happen).

b. Population annealing. An alternative to parallel tempering, population annealing maintains a population of R replicas (typically 10^2 to 10^4) all at the same temperature and same quenched disorder. The temperature is gradually decreased from β_{\min} to 1 via n_{steps} intermediate values. At each temperature step from β_k to β_{k+1} , every replica r is assigned a weight

$$\tau_r(k) = \exp [-(\beta_{k+1} - \beta_k) \mathcal{E}_r] \quad (\text{B7})$$

and the population is resampled (with replacement) according to normalized weights $\tilde{\tau}_r$. The new population is thermalized over several Metropolis updates at the new temperature. The free energy for a given quenched disorder is then directly computed from the cumulative weights

$$F_E = - \sum_{k=1}^{n_{\text{steps}}} \ln \left[\frac{1}{R} \sum_{r=1}^R \tau_r(k) \right]. \quad (\text{B8})$$

Population annealing naturally amplifies low-energy configurations while culling high-energy configurations, making it particularly effective for disordered systems with rough energy landscapes, such as lattice gauge models.

2. Additional simulation details

Parallel tempering simulations were typically executed with 1000–2000 thermalization steps, 5000 to 20000 sweeps (over which the Bennett acceptance ratios were computed), and 10000 to 20000 quenched disorder realizations. 10–20 temperature steps were used for the replicas. Population annealing typically used 200–1000 thermalization steps, 100–800 population size, and 5000 to 20000 disorder realizations.

Errors were computed using jackknifing: for a nonlinear estimator $\hat{\theta}$ computed from n samples, we compute leave-one-out estimates $\hat{\theta}_{-i}$ by excluding each sample in turn. The jackknife variance is $\sigma^2 = \frac{n-1}{n} \sum_i (\hat{\theta}_{-i} - \bar{\theta})^2$. Error bars display the estimated 95% confidence intervals, indicating $\pm 2\sigma$.

Finally, intersection points of logical error rates were computed by taking sample data within the vicinity of the observed crossing point. Weighted least-squares regression (weighted by the sample errors) approximates each distance curve as a straight line, $y = m_i x + b_i$. The intersection point (x_c, y_c) can be found by the overdetermined equation

$$\mathfrak{E}[\mathbf{p}] = (\mathbf{m} \ -\mathbf{1}) \mathbf{p} + \mathbf{b} = \mathbf{0}, \quad \mathbf{p} = \begin{pmatrix} x \\ y \end{pmatrix} \quad (\text{B9})$$

and using least squares to minimize residuals: $\hat{\mathbf{p}}_c = \text{argmin}_{\mathbf{p}} \|\mathfrak{E}[\mathbf{p}]\|^2$. Error bars are estimated using bootstrapping, varying each sample data point using the jackknife variance and then recalculating the estimator.